# Interfacial Morphodynamics of Proliferating Microbial Communities

Alejandro Martínez-Calvo,[1,2,*,†] Carolina Trenado-Yuste,[2,3,*,‡] Hyunseok Lee,[4] Jeff Gore,[4] Ned S. Wingreen,[1,3,5,§] and Sujit S. Datta[6,2,‖]

[1]*Princeton Center for Theoretical Science, Princeton University, Princeton, New Jersey 08544, USA*
[2]*Department of Chemical and Biological Engineering, Princeton University, Princeton, New Jersey 08544, USA*
[3]*Lewis-Sigler Institute for Integrative Genomics, Princeton University, Princeton, New Jersey 08544, USA*
[4]*Physics of Living Systems, Department of Physics, Massachusetts Institute of Technology, Cambridge, Massachusetts 02139, USA*
[5]*Department of Molecular Biology, Princeton University, Princeton, New Jersey 08544, USA*
[6]*Division of Chemistry and Chemical Engineering, California Institute of Technology, Pasadena, California 91125, USA*

(Received 23 October 2023; revised 30 September 2024; accepted 4 December 2024; published 29 January 2025)

In microbial communities, various cell types often coexist by occupying distinct spatial domains. What determines the shape of the interface between such domains—which, in turn, influences the interactions between cells and overall community function? Here, we address this question by developing a continuum model of a 2D spatially structured microbial community with two distinct cell types. We find that, depending on the balance of the different cell proliferation rates and substrate friction coefficients, the interface between domains is either stable and smooth or unstable and develops fingerlike protrusions. We establish quantitative principles describing when these different interfacial behaviors arise and find good agreement with both the results of previous experimental reports as well as new experiments performed here. Our work, thus, helps to provide a biophysical basis for understanding the interfacial morphodynamics of proliferating microbial communities as well as a broader range of proliferating active systems.

DOI: 10.1103/PhysRevX.15.011016

Subject Areas: Biological Physics, Interdisciplinary Physics, Soft Matter

## I. INTRODUCTION

Microorganisms do not typically live in isolation; instead, they inhabit spatially structured multicellular communities, where distinct strains or species occupy specific spatial domains [1–18]. This spatial structure can have important consequences for the functioning and stability of a community. For example, it can influence how the resident microbes proliferate and interact with each other, resist external stressors, and collectively perform biochemical transformations—with crucial implications for biogeochemistry, the environment, food, health, and industry [5,19–45]. Hence, considerable research has focused on studying the different morphologies exhibited by microbial communities.

Laboratory studies often focus on communities growing on two-dimensional (2D) planar substrates, due to both their ease of visualization as well as their relevance to the many natural communities that also grow on surfaces. While motility can also influence how microbes spread through their surroundings, in many natural settings, microbial communities predominantly expand through proliferation, which we, thus, focus on in this work. Under these conditions, it is now well known that a broad array of factors—e.g., differences in competition for nutrients, friction with or adhesion to the underlying substrate, interactions with exogenous or cell-secreted compounds, random fluctuations in proliferation, and mutations [3,5,18,19,33–39,42,46–82]—cause different types of microbes to segregate into monoclonal domains on large scales. But what determines the shape of the *interfaces* between these domains is far less well understood, despite the fact that these interfaces are where the interactions between the different constituents [5,17] take place. In experiments where two species are grown together, they almost always segregate into bullseyelike patterns, with one species localized to an inner core

*These authors contributed equally to this work.
†Contact author: amcalvo@princeton.edu
‡Contact author: ctrenado@princeton.edu
§Contact author: wingreen@princeton.edu
‖Contact author: ssdatta@caltech.edu

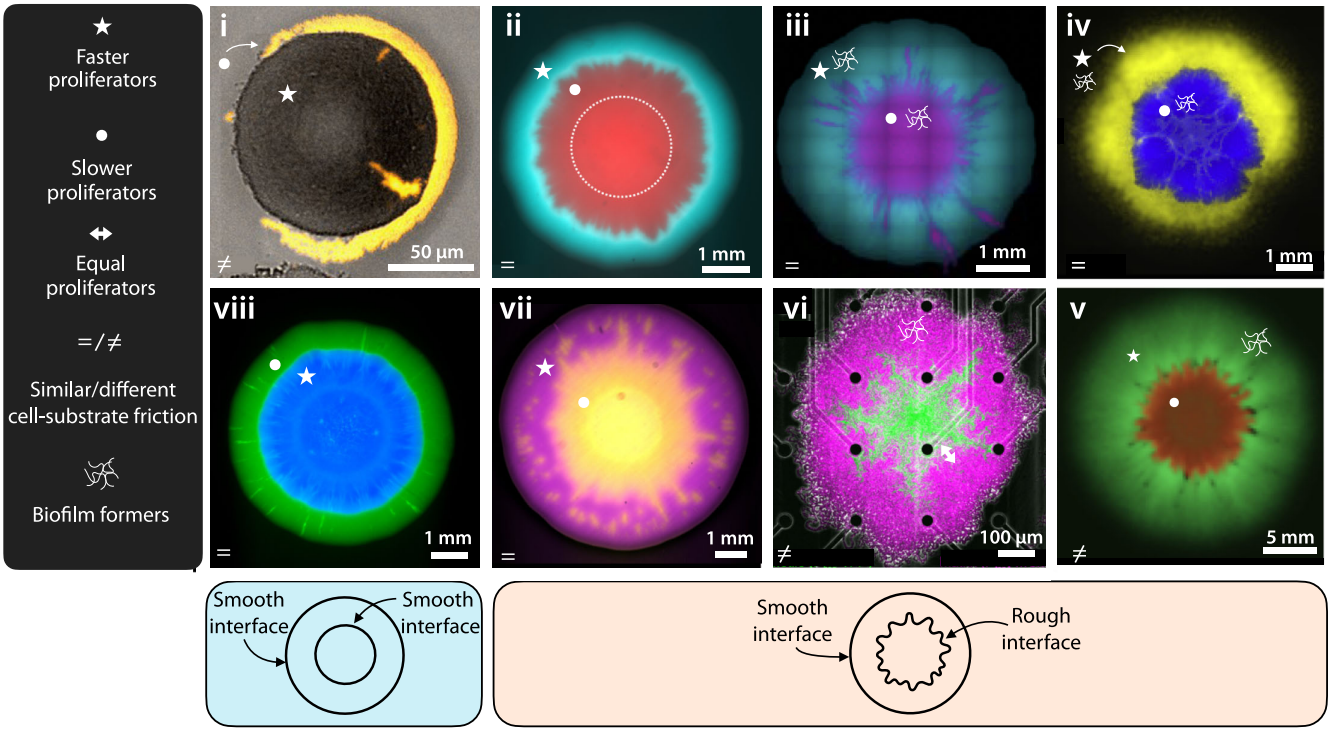


FIG. 1. Experimental images of proliferating 2D core-shell-structured microbial communities on flat surfaces. (i) *Neisseria gonorrhoeae* wild-type (gray inner) and mutant with lower density of type-IV pili (yellow outer) [61]. (ii) Two different strains of *Raoultella planticola* (inner red and outer blue) [79]. (iii) Two different strains of *Pseudomonas putida* (inner magenta and outer blue) [83]. (iv) *Pseudomonas aeruginosa* (inner blue) and *Pseudomonas protegens* (outer yellow) [73]; reprinted with permission from Elsevier. (v) *Bacillus subtilis* mutant (inner red) and wild-type (outer green) [84]; reprinted with permission from Nature Portfolio. (vi) Two different strains of *B. subtilis* (inner green and outer magenta) [77]. (vii) *Pseudomonas rhodesiae* (inner yellow) and *R. planticola* (outer purple), newly studied in this work. (viii) *R. planticola* (inner blue) and *Pantoea agglomerans* (outer green), newly studied in this work. As shown in the left-hand legend, stars (circles) indicate faster (slower) proliferators; equal (unequal) sign in the lower left indicates similar (different) cell-substrate friction between cell types; additional polymer network symbol indicates cells that produce extracellular polymeric substances. As shown in the legends below, the inner and outer interfaces are both smooth in (i) and (viii), whereas the inner interface is wavy and unstable in the other panels.

surrounded by an annular shell of the other. However, the shape of the interface between the two differs from system to system. Sometimes, this interface is smooth [Fig. 1(i)] [61], while in other cases it is wavy with fingerlike protrusions [Figs. 1(ii)–1(vi)], even though the periphery of the outer shell is smooth [59,65,73,77,79,83,84]. Why these differences in interfacial shape arise has thus far remained a puzzle.

Here, we establish a biophysical description of multispecies or strain microbial communities that provides a foundation to help resolve this puzzle. As a first step, we develop a minimal continuum model in 2D that incorporates two essential features of microbes: proliferation and friction with or adhesion to (hereafter referred to as "friction" for brevity) the underlying substrate. Specifically, we consider a community with two different cell types segregated into a core and a shell, each with distinct proliferation rates and cell-substrate friction. Our theoretical analysis and numerical simulations reveal that the interface between these two domains becomes morphologically unstable—exhibiting wavy, fingerlike protrusions as seen in some experiments—when cells in the outer shell proliferate faster or have stronger substrate friction than those in the inner core; otherwise, the interface remains smooth. Moreover, our analysis yields quantitative principles describing when this interfacial instability arises, which we confirm experimentally. Altogether, our work elucidates simple quantitative rules that can help describe the interfacial morphodynamics of microbial communities and potentially other forms of proliferating active matter [85–109].

## II. RESULTS

### A. Model for a proliferating microbial community with two different cell types

Motivated by the experimental observations shown in Fig. 1, we consider a 2D continuum system of two different microbial cell types. Our aim is not to unravel how an initially well-mixed community spatially segregates, but rather to study the morphodynamics of the interface between the different cell types after they have segregated.

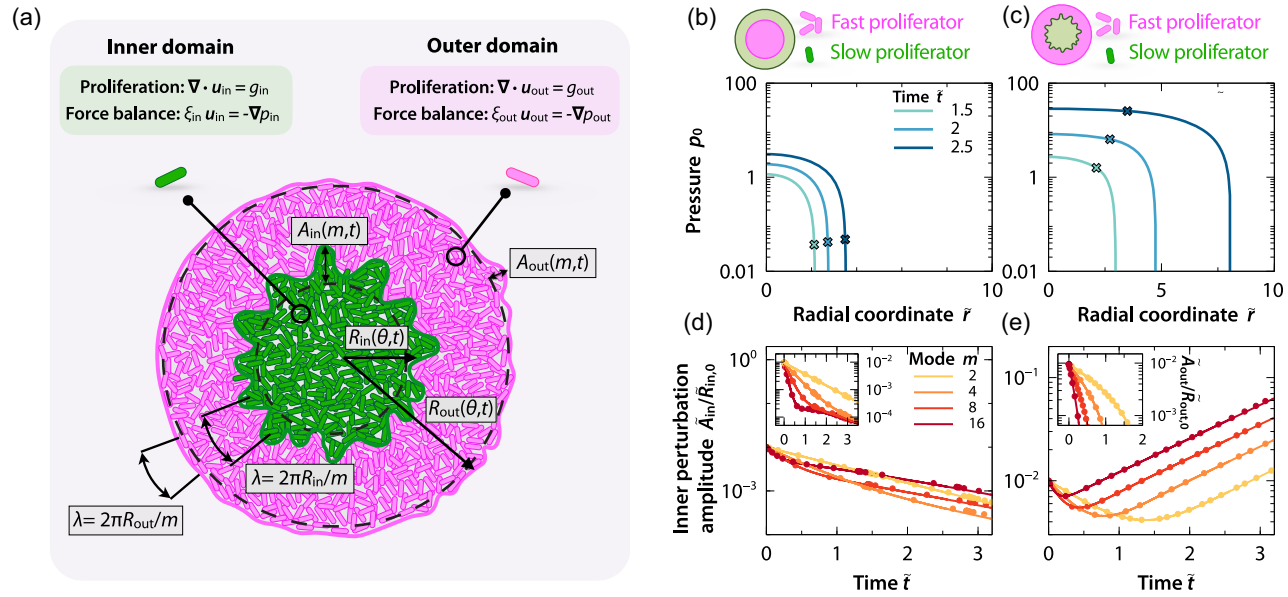


FIG. 2. Mathematical model of a proliferating 2D microbial community with two distinct cell types. (a) Schematic of the 2D continuum system showing an inner domain with one cell type (green) and an outer domain with a different cell type (magenta). $\tilde{A}_{\rm in}$ and $\tilde{A}_{\rm out}$ are the time $\tilde{t}$-dependent amplitudes of shape perturbations with mode number $m$ to the inner and outer interfaces, respectively; $\tilde{R}_{\rm in}$ and $\tilde{R}_{\rm out}$ are the respective azimuthal angle $\theta$-dependent radii of each domain. (b),(c) Base 1D pressure field $\tilde{p}_0$ as a function of radial coordinate $\tilde{r}$ at different times for $\mathcal{R} = 1.05$, $\chi = 1$, and (b) $\mathcal{G} = 0.25$ (inner domain proliferates faster) or (c) $\mathcal{G} = 2.5$ (inner domain proliferates slower). Crosses indicate the position of the interface between the domains. (d),(e) Normalized amplitude of perturbations to the inner interface as a function of time $\tilde{t}$ for the same parameter values as in (b) and (c), respectively; the case in (d) is stable, with perturbation amplitudes that decay over time, whereas the case in (e) is unstable, with perturbation amplitudes that grow with time. The insets in (d) and (e) show similar data but for the outer interface, indicating that it is always stable. Dots are obtained from full numerical simulations of Eqs. (1) and (2), whereas curves are obtained from linear-stability analysis [Eq. (5)], showing excellent agreement between the two. Variables $\tilde{r}$ and $\tilde{t}$ in (b)–(e) are normalized by $R_{\rm in,init}$ and $g_{\rm in}^{-1}$, respectively.

Thus, our starting point is a community that has already segregated into concentric core-shell domains of differing cell types, as schematized in Fig. 2(a). For simplicity, we assume that cells in both domains are effectively incompressible and close packed at a uniform density $\rho$. Moreover, to decouple proliferation from possible spatial variations in the abundance of nutrients, we assume that the community is under nutrient-replete conditions. Therefore, the cells in each domain proliferate uniformly through space at a constant maximal growth rate $g_{\rm i}$, where $\mathrm{i} = \{\mathrm{in}, \mathrm{out}\}$ refers to the inner core and outer shell domains, respectively. However, as shown in Figs. 10 and 11, we find similar results to those presented in the main text when these assumptions of constant density and proliferation rate are relaxed (Appendixes C and D).

The expansion of each domain is caused by cells growing, pushing each other, and proliferating, which can be modeled at the continuum scale as pressure-driven expansion of an "active" fluid [38,39,87,94,110–122]. Hence, we describe the community in terms of a pressure field $p(\boldsymbol{r}, t)$ that is generated by cellular growth and proliferation and a velocity field $\boldsymbol{u}(\boldsymbol{r}, t)$ that is proportional to the local pressure gradient $\boldsymbol{\nabla} p$; here, $\boldsymbol{r}$ and $t$ denote position and time, respectively. The governing equations for each of the two domains are

$$\boldsymbol{\nabla} \cdot \boldsymbol{u}_{\rm i} = g_{\rm i} \quad \text{and} \quad \xi_{\rm i} \boldsymbol{u}_{\rm i} = -\boldsymbol{\nabla} p_{\rm i}, \tag{1}$$

where $0 \le r \le R_{\rm in}$ and $R_{\rm in} \le r \le R_{\rm out}$ describe the inner and outer domains of radius $R_{\rm in}(\theta, t)$ and $R_{\rm out}(\theta, t)$, respectively, and $\theta$ indicates the azimuthal angle [Fig. 2(a)]. Here, $\xi_{\rm i}$ is the friction coefficient between cells in domain i and the underlying substrate; $\xi_{\rm i}$ relates the pressure gradient driving expansion to the expansion speed and is taken to be spatially uniform in each domain [38,123]. As boundary conditions, we impose continuity of pressure and velocity at the inner interface $R_{\rm in}(\theta, t)$, zero pressure at the outer interface $R_{\rm out}(\theta, t)$, and a kinematic condition specifying that the velocity of interface i is equal to the velocity of the fluid at that interface:

$$p_{\rm in} = p_{\rm out} \quad \text{and} \quad \boldsymbol{u}_{\rm in} \cdot \hat{\boldsymbol{n}}_{\rm in} = \boldsymbol{u}_{\rm out} \cdot \hat{\boldsymbol{n}}_{\rm in} \quad \text{at } r = R_{\rm in}(\theta, t), \tag{2a}$$

$$p_{\rm out} = 0 \quad \text{at } r = R_{\rm out}(\theta, t), \tag{2b}$$

$$(\partial_t \boldsymbol{r}_{\rm s,i} - \boldsymbol{u}_{\rm i}) \cdot \hat{\boldsymbol{n}}_{\rm i} \quad \text{at } r = R_{\rm i}(\theta, t), \tag{2c}$$

where $\boldsymbol{r}_{\rm s,i} \equiv R_{\rm i}(\theta, t)\hat{\boldsymbol{e}}_r$ and $\hat{\boldsymbol{n}}_{\rm i}$ are the vectors describing the position of and unit normal to interface i, respectively, and $\hat{\boldsymbol{e}}_r$ and $\hat{\boldsymbol{e}}_\theta$ are the radial and azimuthal unit vectors, respectively.

### B. Dimensionless parameters governing our system

Before solving Eqs. (1) and (2) describing the interfacial morphodynamics, we nondimensionalize these governing equations (Appendix A). To do so, we choose the inverse of the maximal proliferation rate of the inner domain $g_{\mathrm{in}}^{-1}$ as the characteristic timescale, the initial position of the inner interface $R_{\mathrm{in,init}}$ as the characteristic length scale, $g_{\mathrm{in}}R_{\mathrm{in,init}}$ as the corresponding characteristic velocity scale, and $g_{\mathrm{in}}R_{\mathrm{in,init}}^2\xi_{\mathrm{in}}$ as the corresponding characteristic pressure. For ease of notation, all variables presented hereafter are nondimensionalized by these quantities, as indicated by tildes. Nondimensionalizing Eqs. (1) and (2) then reveals three key dimensionless parameters:

$$\mathcal{G} \equiv \frac{g_{\mathrm{out}}}{g_{\mathrm{in}}}: \text{ ratio of maximal proliferation rates,} \tag{3a}$$

$$\chi \equiv \frac{\xi_{\mathrm{out}}}{\xi_{\mathrm{in}}}: \text{ ratio of cell-substrate friction coefficients,} \tag{3b}$$

$$\mathcal{R} \equiv \frac{R_{\mathrm{out,init}}}{R_{\mathrm{in,init}}}: \text{ ratio of initial radii.} \tag{3c}$$

The first two parameters describe differences between the proliferation rates and cell-substrate friction coefficients of the inner core and outer shell domains. The last parameter measures the initial thickness of the outer shell domain. For the results presented in the main text below, we focus on the regime $\mathcal{R} \simeq 1$ often observed in experiments, in which the outer domain has just started to expand. Nonetheless, as shown in Figs. 7 and 8, we find qualitatively similar results when considering larger values of $\mathcal{R}$.

### C. Base solution of our model

Having developed this model of a proliferating two-domain microbial community, we next obtain a one-dimensional (1D) base solution of Eqs. (1) and (2), denoted by the subscript 0. To do so, we enforce that the inner and outer interfaces are circularly symmetric. Thus, velocity and pressure depend on the radial coordinate only, $\tilde{\boldsymbol{u}}_{\mathrm{in},0}(\tilde{r})$ and $\tilde{p}_{\mathrm{in},0}(\tilde{r})$, and the positions of the expanding interfaces are only functions of time, i.e., $\tilde{R}_{\mathrm{i},0}(\tilde{t})$. The corresponding 1D solution describing the velocity, pressure, and interfacial positions is

$$\text{inner velocity field} \quad : \tilde{\boldsymbol{u}}_{\mathrm{in},0} = \frac{\tilde{r}}{2}\hat{\boldsymbol{e}}_r, \tag{4a}$$

$$\text{inner pressure field} \quad : \tilde{p}_{\mathrm{in},0} = \frac{\chi}{4}\left[\mathcal{G}(\tilde{R}_{\mathrm{out},0}^2 - \tilde{R}_{\mathrm{in},0}^2) + \frac{\tilde{R}_{\mathrm{in},0}^2 - \tilde{r}^2}{\chi} - \tilde{R}_{\mathrm{in},0}^2(\mathcal{G}-1)\log\left(\frac{\tilde{R}_{\mathrm{out},0}}{\tilde{R}_{\mathrm{in},0}}\right)\right], \tag{4b}$$

$$\text{inner interface} \quad : \tilde{R}_{\mathrm{in},0} = \exp(\tilde{t}/2); \tag{4c}$$

$$\text{outer velocity field} \quad : \tilde{\boldsymbol{u}}_{\mathrm{out},0} = \frac{\mathcal{G}\tilde{r}^2 + (1-\mathcal{G})\tilde{R}_{\mathrm{in},0}^2}{2\tilde{r}}\hat{\boldsymbol{e}}_r, \tag{4d}$$

$$\text{outer pressure field} \quad : \tilde{p}_{\mathrm{out},0} = \frac{\chi}{4}\left[\mathcal{G}\left(\frac{4\tilde{R}_{\mathrm{out},0}^2}{\chi} - \tilde{r}^2\right) + 2(\mathcal{G}-1)\tilde{R}_{\mathrm{in},0}^2\left(\log(\tilde{r}) - \frac{4\log(\tilde{R}_{\mathrm{out},0})}{\chi}\right)\right], \tag{4e}$$

$$\text{outer interface} \quad : \tilde{R}_{\mathrm{out},0} = \exp\left(\mathcal{G}\tilde{t}/2\right)\sqrt{\exp\left[\tilde{t}(1-\mathcal{G})\right] - 1 + \mathcal{R}^2}. \tag{4f}$$

The pressure gradient driving expansion varies throughout the community and depends on the ratio of proliferation rates $\mathcal{G}$. Two examples are given by Figs. 2(b) and 2(c), which show the time evolution of the radial pressure profile $\tilde{p}_0(\tilde{r})$ when $\mathcal{G} = 0.25$ or $\mathcal{G} = 2.5$ with $\chi = 1$, corresponding to the opposing cases of more rapid proliferation of the inner or outer domains, respectively. In the former case, the pressure decreases radially outward through the inner domain due to its faster proliferation and, thus, is weak in the outer domain. Conversely, in the latter case, the pressure remains high through the entire inner domain due to the faster proliferation around it, decreasing gradually through the outer domain instead. This behavior reflects a fundamental difference between our model and that of an externally driven, passive nonproliferating fluid ($g_{\mathrm{i}} \to 0$), which corresponds to the classic Saffman-Taylor problem that is well known to have an unstable interface [124–131]. In that problem, the base solution has a uniform velocity and a pressure field that remains linear over time, in stark contrast to our model. Given this difference, we next ask: How do the nonuniform pressure gradients and velocity fields arising from microbial proliferation influence the stability of the inner and outer interfaces in our model?

### D. Linear-stability analysis reveals that the balance of proliferation rates helps determine interfacial stability

Having obtained a 1D description of the expansion of both inner and outer domains, we next examine the stability of their interfaces. To this end, we perturb Eqs. (1) and (2) with small-amplitude azimuthal disturbances that can be decomposed into Fourier-like modes: $(\tilde{\boldsymbol{u}}_\mathrm{i}, \tilde{p}_\mathrm{i}, \tilde{R}_\mathrm{i}) = (\tilde{\boldsymbol{u}}_{\mathrm{i},0}, \tilde{p}_{\mathrm{i},0}, \tilde{R}_{\mathrm{i},0}) + \epsilon(\tilde{\boldsymbol{u}}_{\mathrm{i},1}, \tilde{p}_{\mathrm{i},1}, \tilde{A}_\mathrm{i})\exp(im\theta)$, where $\tilde{A}_\mathrm{i}$ is the time-dependent amplitude of a perturbation with azimuthal mode number $m$. Introducing this normal-mode decomposition into Eqs. (1) allows us to obtain $\tilde{\boldsymbol{u}}_{\mathrm{i},1}$, $\tilde{p}_{\mathrm{i},1}$, and $\tilde{A}_\mathrm{i}$ using the boundary conditions given in Eqs. (2). Since the timescale of domain expansion is of the same order as that describing the growth of perturbations, a standard dispersion relation between the perturbation growth rate and $m$ cannot be obtained; the growth or decay of perturbations does not necessarily vary exponentially in time. Instead, interfacial stability is determined by the perturbation amplitudes $\tilde{A}_\mathrm{i}$, which are obtained by solving the coupled system of kinematic equations (2c) at leading order in $\epsilon$:

$$\frac{\mathrm{d}\tilde{A}_\mathrm{i}}{\mathrm{d}\tilde{t}} = \left(\tilde{\boldsymbol{u}}_{\mathrm{i},1}|_{\tilde{R}_{\mathrm{i},0}} + \frac{\mathrm{d}\tilde{\boldsymbol{u}}_{\mathrm{i},0}}{\mathrm{d}\tilde{r}}\bigg|_{\tilde{R}_{\mathrm{i},0}} \tilde{A}_\mathrm{i}\right)\cdot\hat{\boldsymbol{e}}_r, \tag{5}$$

with initial conditions $\tilde{A}_\mathrm{i}(\tilde{t}=0) = \tilde{\epsilon}_\mathrm{i}$. This coupled system of equations does not admit an analytical solution; we, therefore, solve it numerically and examine the time dependence of the normalized perturbation amplitudes $\tilde{A}_\mathrm{i}/\tilde{R}_{\mathrm{i},0}$. If $\mathrm{d}[\tilde{A}_\mathrm{i}(\tilde{t})/\tilde{R}_{\mathrm{i},0}(\tilde{t})]/\mathrm{d}\tilde{t} > 0$, shape perturbations at interface i will grow over time, leading to undulations and the formation of fingerlike protrusions, while if $\mathrm{d}[\tilde{A}_\mathrm{i}(\tilde{t})/\tilde{R}_{\mathrm{i},0}(\tilde{t})]/\mathrm{d}\tilde{t} < 0$, shape perturbations will smooth out over time, yielding a stable, circular interface.

We first explore the two cases shown in Figs. 2(b) and 2(c), which correspond to $\chi = 1$ and $\mathcal{G} = 0.25$ or 2.5, respectively. In the former case, both $\tilde{A}_\mathrm{in}/\tilde{R}_{\mathrm{in},0}$ and $\tilde{A}_\mathrm{out}/\tilde{R}_{\mathrm{out},0}$ decay monotonically over time for all mode numbers $m$, as shown by the curves in Fig. 2(d) (main and inset, respectively). Thus, the more rapid proliferation in the inner domain causes both interfaces—between the inner core and outer shell and at the periphery of the outer shell—to be stable to shape perturbations, smoothing out disturbances and resulting in circular expansion. We confirm this finding using full 2D numerical simulations of Eqs. (1) and (2), with the initial shape of each interface perturbed by the corresponding mode number $m$. The results are shown by the symbols in Fig. 2(d), in excellent agreement with the linear-stability analysis.

We observe dramatically different behavior for the latter case of $\mathcal{G} = 2.5$, corresponding to more rapid proliferation in the outer domain. While $\tilde{A}_\mathrm{out}/\tilde{R}_{\mathrm{out},0}$ again decays over time for all mode numbers $m$ [Fig. 2(e), inset], by contrast in this case, $\tilde{A}_\mathrm{in}/\tilde{R}_{\mathrm{in},0}$ *increases* with time [Fig. 2(e), main]. This striking result from linear-stability analysis is again confirmed by numerical simulations, as shown by the excellent agreement between the symbols and the curves. Thus, while the periphery of the outer shell is stable to shape perturbations, the interface between the inner and outer domains is not—as observed in corresponding experiments (Fig. 1). Moreover, perturbations with larger mode numbers $m$ begin growing sooner than those with smaller mode numbers [different colors in Fig. 2(e)]; that is, short-wavelength perturbations are destabilized faster. The consequences of this interfacial instability are shown by the simulation snapshots in Figs. 3(a)–3(c): while the periphery of the outer domain remains stable, the interface between the inner and outer domains quickly becomes unstable, forming wavy, fingerlike protrusions similar to those seen in the experiments. This behavior is strikingly different from the classic Saffman-Taylor problem, which requires a difference in resistance across an interface (i.e., $\chi \neq 1$) for it to become unstable [124–131]; here, in stark contrast, the interface is unstable even though $\chi = 1$. Altogether, these theoretical and numerical results reveal that the shape of the interface between two different cell types in a microbial community can remain stable or become destabilized, depending on the ratio of the proliferation rates between the two. Performing the same simulations but for an interface between slab-shaped—versus concentric circular—domains yields similar results (Figs. 6 and 8), indicating that this phenomenon is not specific to the circular geometry.

### E. Proliferation transverse to the expansion direction determines interfacial stability

Why is the outer domain always stable? And why does the stability of the interface between the inner and outer domains depend on the ratio of their proliferation rates? Inspecting the profiles of the velocity transverse to the expansion direction in both domains helps to answer these questions. For clarity of visualization, we use simulations of a slab-shaped community with $\mathcal{G} = 2.5$, shown in Figs. 3(e)–3(g).

First, we focus on the outer interface, shown by the magenta line in Figs. 3(e) and 3(g). The outer domain proliferates freely, expanding into empty space without any external resistance; indeed, this is the case for any value of $\mathcal{G}$. Transverse proliferation from the "peaks" of shape perturbations can then fill in the "valleys," smoothing out these perturbations and stabilizing the outer interface [132]—as quantified by the transverse velocities in Fig. 3(e).

We next focus on the interface between inner and outer domains, shown by the green line in Figs. 3(e)–3(g). In principle, transverse proliferation in the inner domain can again stabilize shape perturbations of this interface—which

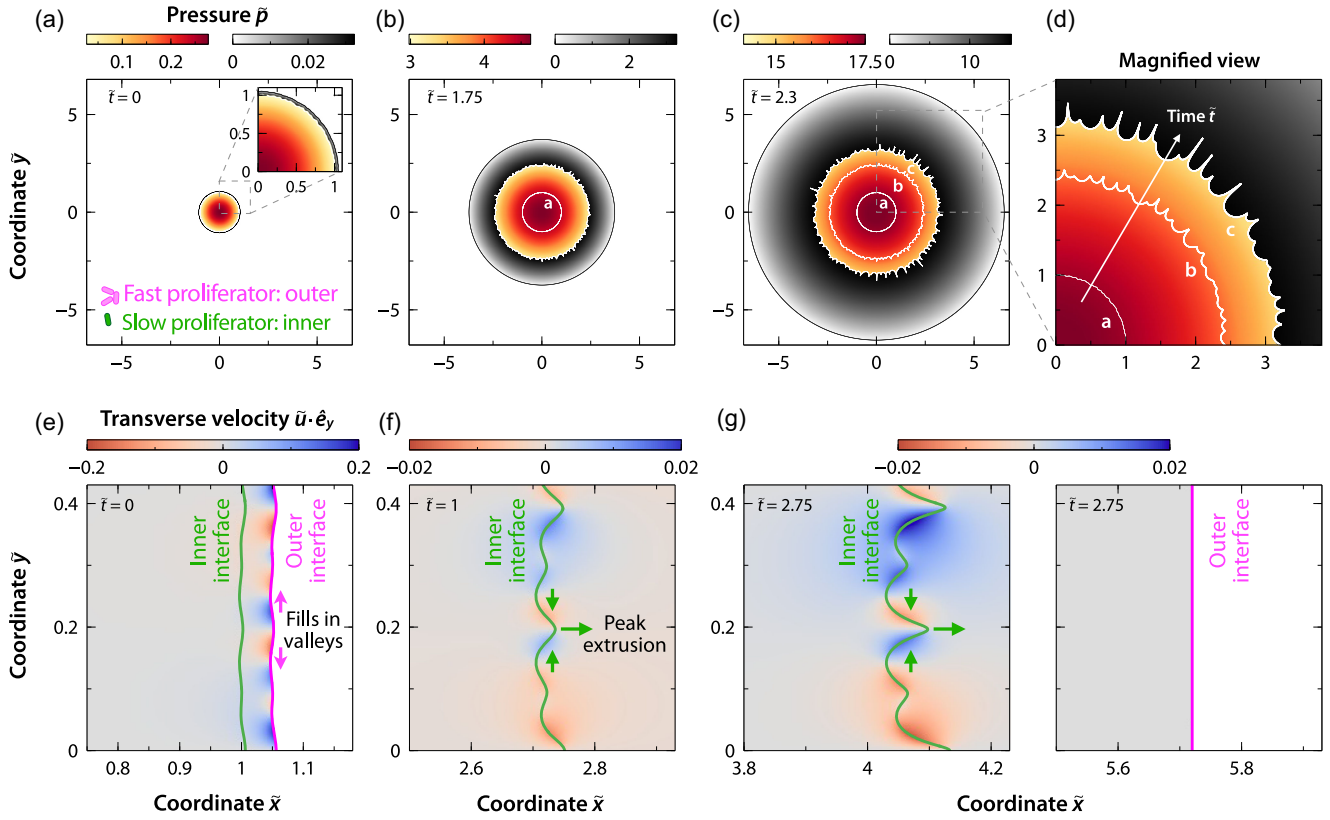


FIG. 3. Numerical simulations reveal that differential proliferation transverse to the expansion direction determines interfacial stability. (a)–(d) Color plots of the pressure field $\tilde{p}(\tilde{\boldsymbol{r}},\tilde{t})$ in the inner and outer domains for $\mathcal{G}=2.5$ (outer domain proliferates faster), $\chi=1$, and $\mathcal{R}=1.05$, at (a) $\tilde{t}=0$, (b) $\tilde{t}=1.75$, and (c),(d) $\tilde{t}=2.3$. (d) shows a magnified view of (c), where white curves indicate the shape of the inner interface at different times. The initial shape of both interfaces is perturbed with random white noise. (e)–(g) Color plots of the transverse velocity $\tilde{\boldsymbol{u}}\cdot\hat{\boldsymbol{e}}_y$ in the inner and outer domains for a slab-shaped community with the same values of $\mathcal{G}$ and $\chi$ as in (a)–(d) and $\mathcal{R}=1.05$ (where here $\mathcal{R}\equiv X_{\mathrm{right,init}}/X_{\mathrm{left,init}}$; see Appendix B), at (e) $\tilde{t}=0$, (f) $\tilde{t}=1$, and (g) $\tilde{t}=2.75$. Transverse proliferation in the outer domain squeezes and extrudes the peaks of shape perturbations, destabilizing the interface. In all panels, variables $(\tilde{x},\tilde{y})$ and time $\tilde{t}$ are normalized by $R_{\mathrm{in,init}}$ and $g_{\mathrm{in}}^{-1}$, respectively; velocity and pressure are then normalized by $g_{\mathrm{in}}R_{\mathrm{in,init}}$ and $g_{\mathrm{in}}R_{\mathrm{in,init}}^2\xi_{\mathrm{in}}$, respectively.

indeed is the case when $\mathcal{G}<1$. However, when the outer domain proliferates faster, $\mathcal{G}>1$, transverse proliferation in the outer domain has a stronger, opposite effect: It squeezes and extrudes the peaks of shape perturbations, as shown by the green arrows in Figs. 3(f) and 3(g), destabilizing the interface.

### F. Model captures the characteristic length and time scales of the instability seen in experiments

To what extent can our theoretical model capture the interfacial morphodynamics in experiments? The experiments in Figs. 1(i)–1(vi) clearly show that the interface between different domains can be stable or unstable depending on the balance of proliferation rates, as our theory predicts. However, our analysis indicates that the exact spatial and temporal features of the instability are sensitive to the initial conditions and total nutrient availability in a given experiment, which were not controlled or reported in these prior studies—precluding quantitative comparison of their interfacial morphodynamics with our theory. So, instead, we perform two new experiments (detailed further in Appendixes E and F) with communities of bacterial species isolated from soil, along with numerical simulations of our model extended to include nutrient limitation (detailed in Appendix D) using input parameters and initial conditions determined directly from the experiments.

In the first experiment, the inner and outer domains are composed of *P. rhodesiae* and *R. planticola*, respectively, with $\mathcal{G}\simeq 1.6>1$ and $\chi\simeq 1$. In this case, we expect the outer interface to be stable but the inner interface to be unstable—just as we find experimentally, as shown in Fig. 1(vii). Indeed, our model captures the full time evolution of the experimental interface shape well, as shown in Fig. 4(a). In the second experiment, the inner and outer domains are composed of *R. planticola* and *P. agglomerans*, respectively, this time with $\mathcal{G}\simeq 0.7<1$

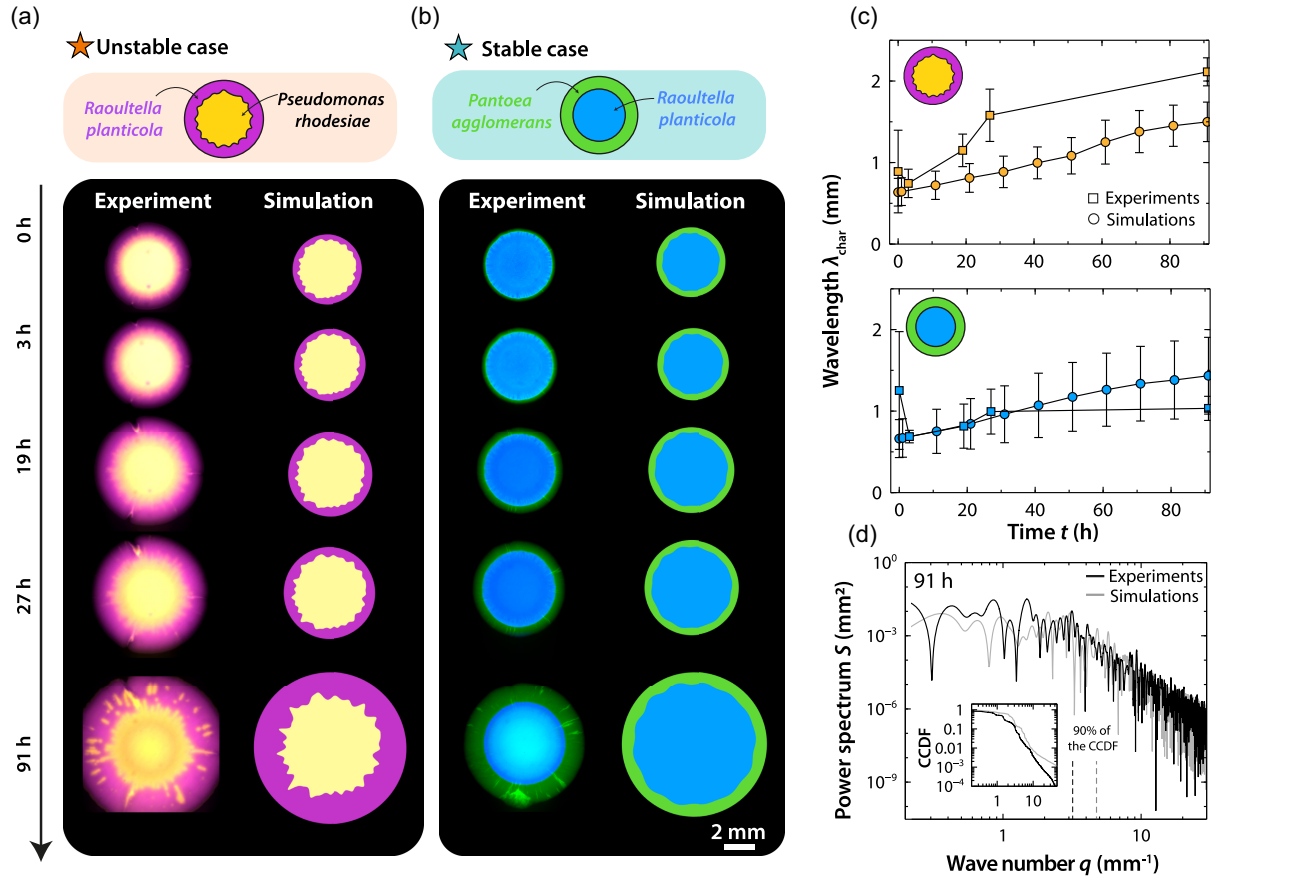


FIG. 4. Model recapitulates interfacial morphodynamics seen in experiments. (a) Left: time evolution of a community composed of *P. rhodesiae* (inner yellow) and *R. planticola* (outer purple), corresponding to $\mathcal{G} \simeq 1.6$ and $\chi = 1$. In this case, the inner interface is unstable. Right: snapshots of the numerical simulations for $\mathcal{G} = 1.6$ and $\chi = 1$ (detailed in Appendix E). (b) The same as in (a) but for a community composed of *R. planticola* (inner blue) and *P. agglomerans* (outer green), corresponding to $\mathcal{G} \simeq 0.7$ and $\chi = 1$. In this case, the inner interface is stable. Right: snapshots of the numerical simulations for $\mathcal{G} = 0.7$ and $\chi = 1$ (detailed in Appendix E). (c) Characteristic wavelength $\lambda_{\mathrm{char}}$ of the inner interface as a function of time obtained from the experiments (squares) and simulations (circles) shown in (a) (top) and (b) (bottom). The experimental error bars represent the standard deviation of three replicates, while the simulation error bars represent the standard deviation of three different simulations, each starting with different interface-perturbation mode numbers to add variability in the initial conditions. (d) Power spectrum of spatial fluctuations of the inner interface radius as a function of the wave number $q$ at time $t = 91$ h in both experiments (black) and simulations (gray) for the unstable case shown in (a). The vertical lines indicate the wave numbers below which 90% of the power is found in experiments and simulations. The inset shows the complementary cumulative distribution function as a function of $q$.

and $\chi \simeq 1$. In this case, we expect both inner and outer interfaces to be stable—which our experiment again corroborates, as shown in Fig. 1(viii). Moreover, our model again captures the full time evolution of the experimental interface shape well, as shown in Fig. 4(b).

To more quantitatively compare the experiments and theory, we compute the power spectrum of spatiotemporal fluctuations of the inner interface radius $R_{\mathrm{in}}(s,t)$ measured with respect to the arclength $s$ and as a function of time $t$: $S(q,t) = |s_{\mathrm{end}}^{-1} \int_0^{s_{\mathrm{end}}} \mathrm{d}s [R_{\mathrm{in}}(s,t) - \langle R_{\mathrm{in}} \rangle_s(t)] \exp(-iqs)|^2$, where $q = 2\pi/\lambda$ is the wave number of a given mode of wavelength $\lambda$. We observe fluctuations over a broad range of $q$ but with most of the power concentrated in a narrow range of modes. Hence, we define the characteristic wavelength of the instability $\lambda_{\mathrm{char}}$ as the wavelength above which 90% of the total integrated value of $S(q,t)$ is observed. As shown in Fig. 4(c), we find good agreement for the time evolution of $\lambda_{\mathrm{char}}$ between simulations (circles) and experiments (squares), for both the unstable (orange) and stable (blue) cases. Both experiments and simulations show an increasing $\lambda_{\mathrm{char}}$ over time as the colony expands, which makes sense intuitively since $\lambda \sim 2\pi R/m$. Moreover, as exemplified in Fig. 4(d) for the unstable case, the final morphology of the inner interface is similar in both simulations and experiments, as shown by the similar power spectra of the fluctuations. Taken together, these data demonstrate that, despite the simplicity of our theoretical model, it can quantitatively capture the key length and timescales of the instability seen in experiments.

### G. A morphological state diagram unifies the influence of proliferation and friction in determining interfacial stability

Thus far, we have focused on the influence of differences in the proliferation rate $g_i$ on interfacial morphodynamics, for inner and outer domains with identical cell-substrate friction ($\chi = 1$). However, the different cell types may also differ in their friction coefficient $\xi_i$ due to, e.g., differences in adhesin expression or production of extracellular polymeric substances (EPS). Hence, we next perform linear-stability analysis over a broad range of $\mathcal{G}$ and $\chi$.

Our results are summarized by the state diagram in Fig. 5, which shows the stability of the interface between inner and outer domains as a function of $\mathcal{G}$ and $\chi$, based on the long-time growth rate of perturbations of different mode numbers $m$. The corresponding pressure profiles of the base solution are shown in Fig. 9. The teal shading in Fig. 5 indicates the region of $(\mathcal{G},\chi)$ parameter space in which both inner and outer interfaces remain stable for all $m$, as in Fig. 2(d), due to transverse proliferation from peaks of shape perturbations filling in valleys. Conversely, the dark orange shading indicates the region in which the outer interface remains stable, but the inner interface becomes unstable, for all $m$, as in Figs. 2(e) and 3. In this case, the increased friction in the outer domain ($\chi > 1$) drives squeezing and extrusion of shape perturbations of the inner interface as in Fig. 3.

The light orange shading in the lower right ($\mathcal{G} > 1$, $\chi < 1$) indicates an intriguing region in which the outer interface always remains stable, but the inner interface exhibits $m$-dependent stability, with each solid curve indicating the stability boundary for a given mode $m$; above and right of each such curve, the inner interface is unstable to that mode. In this case, the increased friction experienced by the inner domain helps to compensate for the squeezing and extrusion of perturbations at the inner interface induced by more rapid proliferation in the outer domain. The corresponding light orange shading in the upper left ($\mathcal{G} < 1$, $\chi > 1$) indicates another intriguing region in which both the inner and outer interfaces exhibit $m$-dependent stability; above and right of each such curve, both interfaces are unstable to that mode $m$. In this case, the stabilizing sideways proliferation of the inner domain is hindered by the increased friction in the outer domain. Moreover, peaks of perturbations at the inner interface proliferate faster than valleys, ultimately pushing the outer interface to also become unstable.

### H. Theoretical predictions recapitulate experimental observations across diverse microbial systems

The state diagram in Fig. 5 quantifies our central finding: that, depending on the proliferation rate and friction ratios $\mathcal{G}$ and $\chi$, the inner and outer interfaces of a two-domain microbial community can be stable, remaining circular, or unstable, generating fingerlike protrusions that continue to grow. As shown in Fig. 4, our theoretical model despite its simplicity quantitatively captures the full interfacial morphodynamics observed in our experiments; these cases are shown by the stars in Fig. 5. As expected, the experiments with $\mathcal{G} \simeq 1.6 > 1$ and $\mathcal{G} \simeq 0.7 < 1$ fall in the unstable and stable regimes of the state diagram, respectively. Having

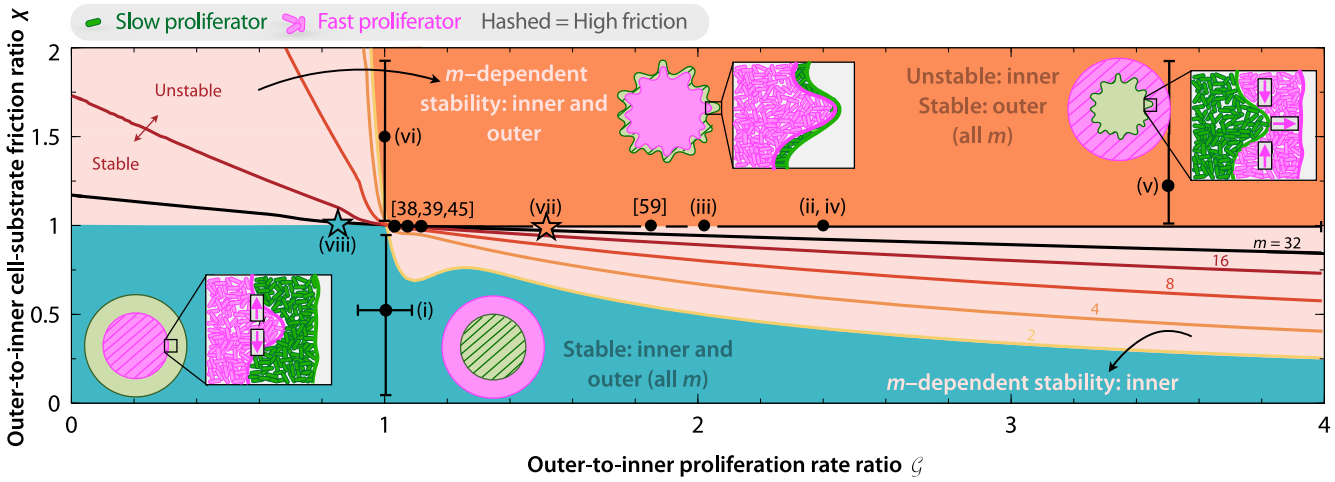


FIG. 5. State diagram describes how the balance of differential proliferation and friction determines interfacial stability, in agreement with experiments. Colors show predicted interfacial stability, based on the long-time growth rate of perturbations of different mode number $m$, as a function of $\mathcal{G}$ and $\chi$ for a community with initial radius ratio $\mathcal{R} = 1.05$. Curves indicate the stable-unstable transition for different $m$ modes. Points (i)–(viii) denote the experiments in Fig. 1. Additionally, the stars in (vii) and (viii) highlight the experiments in Figs. 4(a) and 4(b), respectively. Horizontal error bar reflects the reported uncertainty in proliferation rates, while vertical large errors bars indicate that we are unable to quantify the exact values of $\chi$ for experiments (i), (v), and (vi) and simply know that $\chi < 1$ for (i) and $\chi > 1$ for (v) and (vi). The $m = 2$ curve shows an unusual nonmonotonic variation at $(\mathcal{G},\chi) \approx (1.1, 0.7)$; we do not see this nonmonotonicity for either slab-shaped communities or circular communities with a larger initial outer thickness, as shown in Figs. 6 and 7, respectively, indicating that this behavior arises from geometric effects due to curvature.

established this agreement, we next ask: to what extent do our model predictions also capture experimental observations by others across a broader range of microbial systems? To address this question, we examine the experiments shown in Figs. 1(i)–1(vi), as detailed in Appendix E.

Figure 1(i), taken from Ref. [61], shows a community of *N. gonorrhoeae* where both inner and outer interfaces are stable. Here, the outer domain is comprised of mutant cells with a smaller density of type-IV pili, thereby reducing cell-substrate friction, compared to the wild-type cells in the interior domain; that is, $\mathcal{G} \simeq 1$ and $\chi < 1$. As shown in this region in Fig. 5, our theory predicts that both inner and outer interfaces are indeed stable, as observed experimentally.

Figures 1(ii)–1(iv), taken from Refs. [73,79,83], show communities of bacteria [(ii)–(iv)] or yeast (Refs. [38,39,45,59]) where the outer interface remains stable but the inner interface is unstable. Additional examples were reported in Refs. [38,39,45,59]. In all these cases, no differences between the inner and outer cell types with respect to cell-substrate friction were reported ($\chi \simeq 1$). Rather, in all these experiments, the outer cells proliferated faster than those in the inner domain; that is, $\mathcal{G} > 1$. As shown by the points in Fig. 5, our theory predicts that the outer interface is stable, but the inner interface is unstable, as observed in the experiments.

Figure 1(v), taken from Ref. [84], shows a community of *B. subtilis* where the outer interface remains stable but the inner interface is unstable. Here, the outer strain also proliferated at a higher rate than the inner ($\mathcal{G} > 1$). In addition, cells in the outer domain produced EPS, increasing the cell-substrate friction, unlike those in the inner domain that did not; therefore, $\chi > 1$. As shown by the point in Fig. 5, our theory predicts that the outer interface is stable but the inner interface is unstable, just as in the experiments.

Figure 1(vi), taken from Ref. [77], also shows a community of *B. subtilis* where the outer interface remains stable but the inner interface is unstable. In this case, however, both strains proliferated at a similar rate ($\mathcal{G} \simeq 1$), while cells in the outer domain also produce EPS, unlike those in the inner domain, implying $\chi > 1$. As shown in this region in Fig. 5, our theory predicts that the outer interface is stable but the inner interface is unstable, as observed experimentally.

Taken altogether, these analyses show that our theory successfully rationalizes experimental observations of interfacial stability, both published in previous literature and newly performed in this work, across a broad range of microbial species.

## III. DISCUSSION

By combining theory, simulation, and experiment, we have established a biophysical description of the morphodynamics of interfaces between domains of two different cell types in a microbial community. For the commonly observed core-shell segregation of two cell types, we find that the balance of the different proliferation rates ($\mathcal{G} \equiv g_{\text{out}}/g_{\text{in}}$) and cell-substrate friction coefficients ($\chi \equiv \chi_{\text{out}}/\chi_{\text{in}}$) plays a pivotal role in determining interfacial stability. When $\mathcal{G}$ and $\chi$ are small, valleys in an interface are transversely filled in by adjacent peaks, resulting in a stable, smooth interface. By contrast, when $\mathcal{G}$ and $\chi$ are large, transverse squeezing from valleys causes peaks to become extruded into fingerlike protrusions, resulting in an unstable, wavy interface—providing an active matter counterpart to the classic Saffman-Taylor instability exhibited by passive fluid interfaces [124–131]. Notably, our theory quantitatively captures the results of both previously published experiments, as well as new experiments performed here, across a range of different bacterial and yeast strains [59,73,77,79,83], as well as in different geometries. We, therefore, expect that our findings will be generally applicable.

We necessarily make several simplifications and assumptions in formulating our theoretical description. For example, our continuum description neglected orientational ordering of cells. While adjacent cells in the population can indeed align with each other, potentially giving rise to larger-scale orientational ordering in the population, previous work has shown that such ordering persists only over at most approximately tens of cell body lengths [133]—over an order of magnitude smaller than the characteristic colony length scales that our work focuses on, approximately hundreds to thousands of cell body lengths. Therefore, we expect that such ordering will potentially influence colony morphodynamics at length scales smaller than we focused on here, and exploring the influence of this additional complexity will be a relevant direction for future work. We also assume that the cell proliferation rate $g$, friction coefficient $\xi$, and density $\rho$ are constant throughout each distinct domain [114,133–136]. Investigating the role of nonuniform cell-substrate friction and cell density on community morphodynamics will be a useful future extension of our work. Additionally, there may be nontrivial couplings between the pressure $p$ and $g$ [137–139], as well as nontrivial features of cellular and community rheology or osmotic effects [53,140,141], that could change the form of Eq. (1) and potentially give rise to out-of-plane proliferation into the third dimension [54,142,143]. Importantly, in all the experiments we focus our analysis on and in many experiments of colony growth, the colony vertical thickness (at most approximately tens of cell body lengths) is much smaller than the radial length scale (exceeding approximately hundreds to thousands of cell body lengths), and no out-of-plane deformations—such as buckling or wrinkling—are observed. Because of this separation of length scales, our analysis follows the established framework of lubrication theory in fluid mechanics, with all quantities averaged through the out-of-plane direction. This approach has been applied to successfully describe microbial colonies in other contexts [38,39,85–87,94,110–122] and other living systems [85–102,108,109,139,144–146]. However, as noted above,

deformations in 3D certainly play a role in many cases. Moreover, while our model considers different cell types that interact with each other purely mechanically, they may also regulate each other's proliferation through other means, e.g., via cell-secreted factors such as metabolic byproducts, autoinducers, and toxins [147–150]. Finally, we note that here we focus on experiments in which the individual cell types are either nonmotile or proliferate on stiff, adherent substrates on which they cannot swim or swarm; thus, motility effects are abrogated in these studies by design. However, we expect that motility effects such as chemotaxis and swarming will increasingly influence large-scale colony morphodynamics in other settings, such as on less stiff or adherent substrates [72,74,107,151]. Incorporating these complexities into the framework developed here will be a useful direction for future work.

What could the biological implications of the interfacial morphodynamics revealed by our work be? The emergence of wavy fingers at the interface between different cell types could be beneficial for the community. By increasing the length of the interface, this interfacial instability may promote cooperative metabolic interactions between the two domains. Cells located at fingerlike protrusions may have better access to any beneficial by-products released by the other cell type. This instability may also facilitate short-range communication between cells through diffusible signals and metabolites [147–150] or even long-range communication via ion channels [21,24,25]. On longer timescales, the increase in interfacial length caused by this instability could also facilitate gene transfer between the different cell types, with possible implications for, e.g., the spread of antibiotic resistance [152]. Hence, our work suggests the tantalizing hypothesis that, by regulating cell-scale proliferation or friction, different cell types may be able to regulate large-scale community structure and functioning. Conversely, however, this effect could also be harmful to a community by promoting exposure of the cells to external stressors. Testing these ideas will be an important direction for future research.

By elucidating simple quantitative principles that can help describe the interfacial morphodynamics of microbial communities, our work could also help guide efforts to engineer microbial systems with programmed structures and functions [69,104–106,153]. More broadly, our theoretical framework is not restricted to microbial systems but could be extended to other forms of proliferating active matter, such as mammalian tissues, which can also be described at the continuum scale as "active" fluids whose expansion is driven by a pressure gradient generated by cellular growth and proliferation, as formulated by our model. Therefore, we expect that our model could be extended—e.g., by incorporating the polarity and motility of mammalian cells—to describe phenomena such as the occurrence of fingering instabilities in colliding epithelial monolayers, morphogenesis of mammalian tissues, and shapes of growing tumors [85–102,108,109,139,144–146]. Exploring such extensions to describe interfacial morphodynamics more generally in other proliferating multicellular systems will be an exciting direction for future work.

## ACKNOWLEDGMENTS

A. M.-C. acknowledges support from the Princeton Center for Theoretical Science, the Center for the Physics of Biological Function, and the Human Frontier Science Program through Grant No. LT000035/2021-C. C. T.-Y. acknowledges support from the Damon Runyon Cancer Research Foundation through the 2023 Damon Runyon Quantitative Biology Fellowship (DRQ-17-23), the New Jersey Department of Health, the Division of Office of Research Initiatives, and the New Jersey Commission on Cancer Research (NJCCR) through the 2023 NJCCR Postdoctoral Research Grant. H. L. and J. G. acknowledge support from MIT Physics of Living Systems and the Sloan Foundation through Grant No. G-2021-16758. N. S. W. acknowledges support from the National Science Foundation (NSF) through the Center for the Physics of Biological Function PHY-1734030 and the National Institutes of Health through Grant No. R01 GM082938. S. S. D. acknowledges support from NSF Grant No. CBET-1941716, No. DMR-2011750, and No. EF-2124863, as well as the Camille Dreyfus Teacher-Scholar and Pew Biomedical Scholars Programs, the Eric and Wendy Schmidt Transformative Technology Fund, and the Princeton Catalysis Initiative. We thank Howard A. Stone and Hongbo Zhao for thoughtful discussions.

A. M.-C. and C. T.-Y. carried out the theoretical calculations and numerical simulations and contributed equally to this work; H. L. carried out the experiments; A. M.-C., C. T.-Y., N. S. W., and S. S. D. designed the overall study and analyzed the data; all authors contributed to writing the paper.

## APPENDIX A: DIMENSIONLESS GOVERNING EQUATIONS

Here, we present the dimensionless version of Eqs. (1) and (2), obtained using the characteristic scales described in the main text. In particular, we express the system of equations in terms of the proliferation pressure field, which yields

volume conservation :

$$\nabla^2 \tilde{p}_{\mathrm{in}} = -1, \quad \text{at } 0 \le \tilde{r} \le \tilde{R}_{\mathrm{in}}, \tag{A1}$$

$$\nabla^2 \tilde{p}_{\mathrm{out}} = -\mathcal{G}\chi, \quad \text{at } \tilde{R}_{\mathrm{in}} \le \tilde{r} \le \tilde{R}_{\mathrm{out}}; \tag{A2}$$

stress balance :

$$\tilde{p}_{\mathrm{in}} = \tilde{p}_{\mathrm{out}}, \quad \text{at } \tilde{r} = \tilde{R}_{\mathrm{in}}, \tag{A3}$$

$$\tilde{p}_{\mathrm{out}} = 0, \quad \text{at } \tilde{r} = \tilde{R}_{\mathrm{out}}; \tag{A4}$$

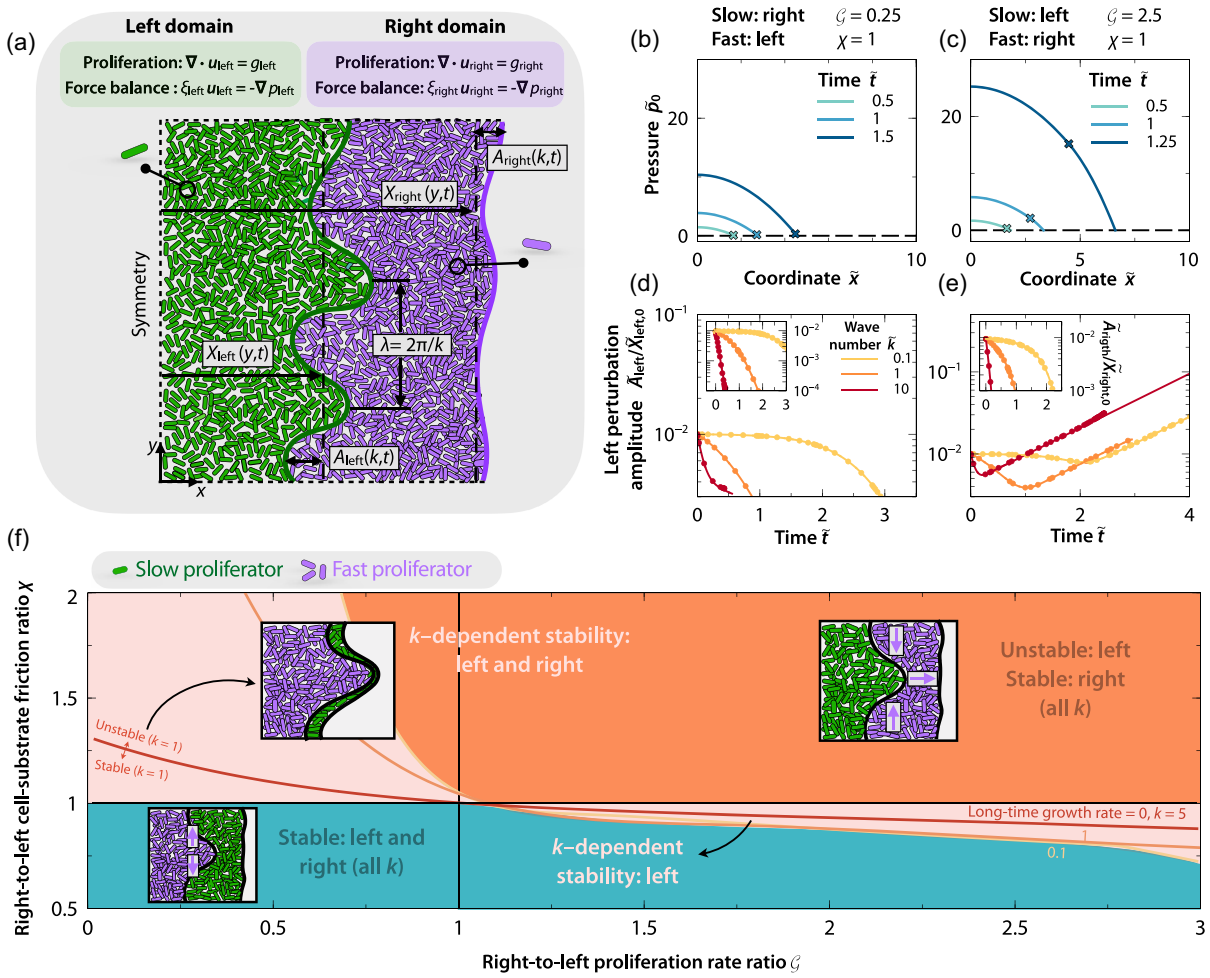


FIG. 6. (a) Schematic of slab-shaped 2D continuum system showing a left domain with one cell type (green) and a right domain with a different cell type (magenta). $\tilde{A}_{\text{left}}$ and $\tilde{A}_{\text{right}}$ are the time $\tilde{t}$-dependent amplitudes of shape perturbations with wave number $k$ to the inner and outer interfaces, respectively; $\tilde{X}_{\text{left}}$ and $\tilde{X}_{\text{right}}$ are the respective $\tilde{y}$-dependent widths of each domain. (b)–(e) are identical to the panels in Fig. 2 but for this community in this new coordinate system. (f) State diagram identical to Fig. 5 but for this community in this new coordinate system, for perturbations indexed by wave number $\tilde{k}$. These calculations are for $\mathcal{R} = 1.05$, where here $\mathcal{R} \equiv X_{\text{right,init}}/X_{\text{left,init}}$. As shown by all these panels, the results for a proliferating microbial community in a slab geometry are similar to those obtained for a circular geometry.

continuity of velocity :

$$\chi \nabla \tilde{p}_{\text{in}} \cdot \hat{\boldsymbol{n}}_{\text{in}} = \nabla \tilde{p}_{\text{out}} \cdot \hat{\boldsymbol{n}}_{\text{in}}, \quad \text{at } \tilde{r} = \tilde{R}_{\text{in}}; \tag{A5}$$

kinematic condition :

$$(\partial_{\tilde{t}} \tilde{\boldsymbol{r}}_{\text{s,in}} + \nabla \tilde{p}_{\text{in}}) \cdot \hat{\boldsymbol{n}}_{\text{in}} = 0, \quad \text{at } \tilde{r} = \tilde{R}_{\text{in}}, \tag{A6}$$

$$(\partial_{\tilde{t}} \tilde{\boldsymbol{r}}_{\text{s,out}} + \chi^{-1} \nabla \tilde{p}_{\text{out}}) \cdot \hat{\boldsymbol{n}}_{\text{out}} = 0, \quad \text{at } \tilde{r} = \tilde{R}_{\text{out}}. \tag{A7}$$

## APPENDIX B: SLAB-SHAPED COMMUNITIES

Here, we investigate the same model as that presented in the main text but for a community that is slab-shaped, as schematized in Fig. 7, rather than circular. To this end, we first obtain a 1D solution of Eqs. (1) and (2) enforcing that the expanding interfaces of both proliferating domains are purely planar; i.e., all the variables depend on the $\tilde{x}$ coordinate only, and the positions of both interfaces are functions of time $\tilde{t}$ only. The 1D solution reads

$$\text{left velocity field: } \tilde{\boldsymbol{u}}_{\text{left},0} = \tilde{x}\hat{\boldsymbol{e}}_x, \tag{B1}$$

$$\text{left pressure field: } \tilde{p}_{\text{left},0} = \frac{1}{2}[\tilde{X}^2_{\text{left},0} - \tilde{x}^2 + \chi(\tilde{X}_{\text{left},0} - \tilde{X}_{\text{right},0})[(\mathcal{G}-2)\tilde{X}_{\text{left},0} - \mathcal{G}\tilde{X}_{\text{right},0}]], \tag{B2}$$

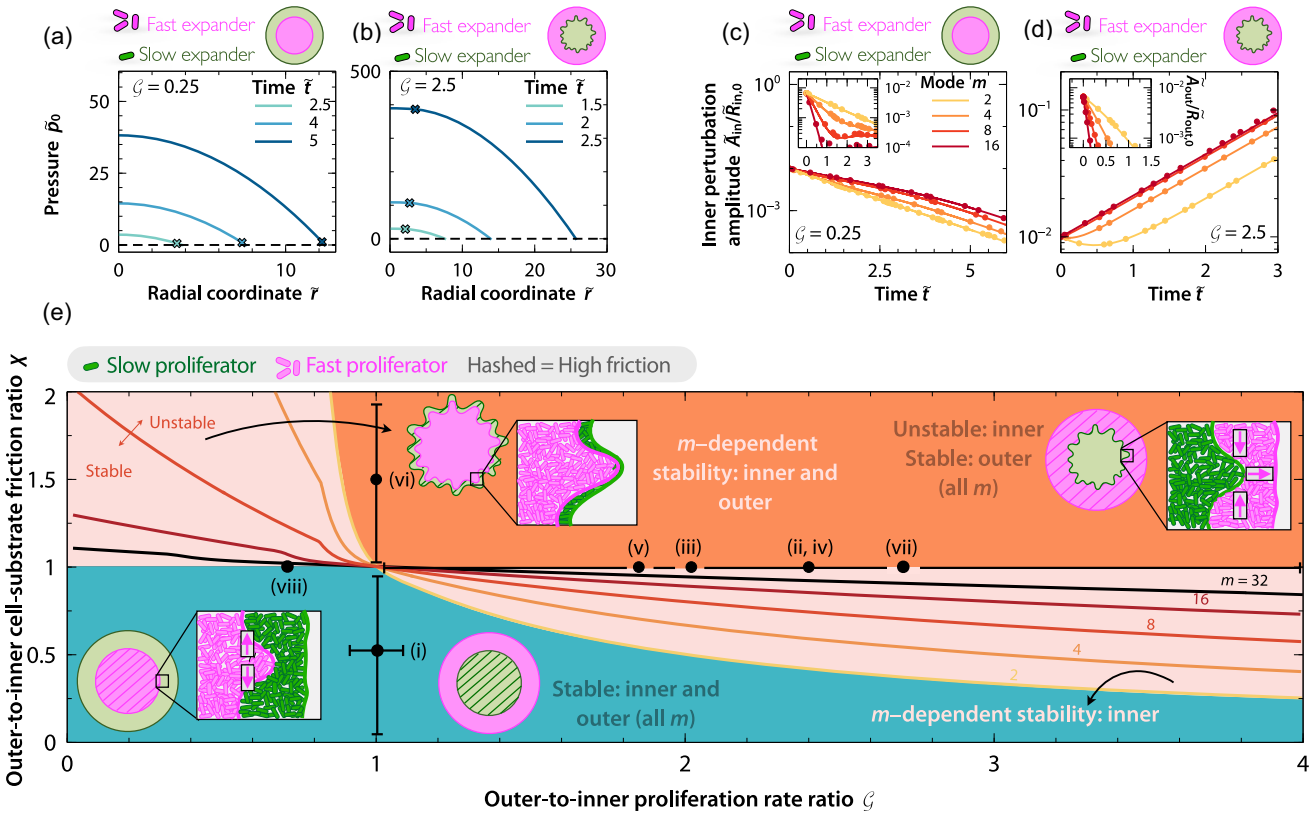


FIG. 7. Model predictions for a community with $\mathcal{R} = 1.5$ show qualitatively similar results to those for the community with $\mathcal{R} = 1.05$ presented in the main text. (a)–(d) are identical to (b)–(e) in Fig. 2 but for $\mathcal{R} = 1.5$. Similarly, (e) is identical to Fig. 5 but for $\mathcal{R} = 1.5$.

$$\text{left interface} \quad : \tilde{X}_{\text{left},0} = \exp(\tilde{t}), \tag{B3}$$

$$\text{right velocity field} : \tilde{\boldsymbol{u}}_{\text{right},0} = \mathcal{G}\tilde{x} + (1-\mathcal{G})\tilde{X}_{\text{left},0}\hat{\boldsymbol{e}}_x, \tag{B4}$$

$$\text{right pressure field} : \tilde{p}_{\text{right},0} = \frac{\chi}{2}(\tilde{X}_{\text{right},0} - \tilde{x})[2\tilde{X}_{\text{left},0} + \mathcal{G}(\tilde{x} - 2\tilde{X}_{\text{left},0} + \tilde{X}_{\text{right},0})], \tag{B5}$$

$$\text{right interface} \quad : \tilde{X}_{\text{right},0} = \exp(\tilde{t}) + \exp(\mathcal{G}\tilde{t})(\tilde{X}_{\text{right,init}} - 1). \tag{B6}$$

To perform a linear-stability analysis of the above 1D solution, we perturb Eqs. (1) and (2) by small-amplitude disturbances, which are decomposed into Fourier-like modes, i.e., $(\tilde{\boldsymbol{u}}_i, \tilde{p}_i, \tilde{R}_i) = (\tilde{\boldsymbol{u}}_{i,0}, \tilde{p}_{i,0}, \tilde{X}_{i,0}) + \epsilon(\tilde{\boldsymbol{u}}_{i,1}, \tilde{p}_{i,1}, \tilde{A}_i)\exp(i\tilde{k}\tilde{y})$, where $\tilde{k}$ is the wave number of perturbations along the $\tilde{y}$ direction, $\tilde{A}_i$ denotes the time-dependent perturbation amplitude of the expanding interfaces, and $i = \{\text{left}, \text{right}\}$. As described in the main text for the circular case, we first solve $\tilde{\boldsymbol{u}}_{i,1}$ and $\tilde{p}_{i,1}$ subject to boundary conditions [Eq. (2)], and then $\tilde{A}_i$ are obtained by solving the kinematic condition at leading order in $\epsilon$ [Eq. (5)]:

$$\frac{d\tilde{A}_i}{d\tilde{t}} = \left(\tilde{\boldsymbol{u}}_{i,1}|_{\tilde{X}_{i,0}} + \left.\frac{d\tilde{\boldsymbol{u}}_{i,0}}{d\tilde{x}}\right|_{\tilde{X}_{i,0}} \tilde{A}_i\right) \cdot \hat{\boldsymbol{e}}_x, \tag{B7}$$

with initial conditions $\tilde{A}_i(\tilde{t} = 0) = \tilde{\epsilon}_i$. Equivalently to the circular geometry, this coupled system of equations does not admit an analytical solution; we, therefore, solve it numerically and examine the time dependence of the normalized perturbation amplitudes $\tilde{A}_i/\tilde{X}_{i,0}$. The results of the linear-stability analysis are summarized in Fig. 7, equivalently to Fig. 2 for the circular case, yielding the same results up to metric factors.

## APPENDIX C: THE MORPHOLOGICAL INSTABILITY IS NOT AFFECTED BY NONUNIFORM CELL DENSITY

The relative density of the different cell types is an additional control parameter that can influence the shapes of interfaces between cell types. However, as noted in,

e.g., Ref. [84], this parameter primarily influences the *initial* spatial organization of the different cell types, since the cells need to reach a close-packed uniform density before their domains continue to expand radially outward. That is, when the two distinct cell types have dissimilar densities, the colony may not segregate into the initial core-shell structure that our work focuses on but may instead organize into a more complex configuration. In future, it would be interesting to study why these more complex configurations initially arise and their influence on the morphodynamics of mixed communities.

Moreover, Ref. [84] also notes that, when a coculture of two distinct cell types does start from an initial core-shell structure, the long-time morphodynamics of the interface between cell types are expected to be insensitive to the relative cell density. We directly test this hypothesis by performing numerical simulations of our model. In particular, here we consider the case in which cell density $\rho_i(\boldsymbol{r}, t)$ is not uniform. Hence, the mass and momentum conservation equations read

$$\partial_t \rho_i + \boldsymbol{\nabla} \cdot (\rho_i \boldsymbol{u}_i) = g_i \rho_i \quad \text{and} \quad \mu_i \rho_i \boldsymbol{u}_i = -\boldsymbol{\nabla} p_i, \tag{C1}$$

where $\mu_i$ is the cell-substrate friction coefficient per unit density. To solve Eq. (C1), the relationship between the pressure and density fields must be specified. For simplicity, we follow Ref. [133] and consider the simplest possible relation, i.e., $p_i(\rho_i) = G_i(\rho_i/\rho_{i,un} - 1)$, where $\rho_{i,un}$ is an uncompressed density of closely packed cells (i.e., $p_i = 0$) and $G_i$ is a coefficient relating pressure and cell density that reflects the elastic modulus of cells [110]. Equations equivalent to Eq. (C1) but with different pressure-density relationships have been previously employed to model colonies of bacteria [110,133,154] and eukaryotic cells [89,155,156]. Equation (C1) can be simplified to a reaction-diffusion equation for the density, $\partial_t \rho_i = (\mu_i \rho_{i,un})^{-1} \boldsymbol{\nabla}^2 \rho_i + \rho_i g_i$, where the expanding interfaces move according to $\boldsymbol{u}_i = -G_i \boldsymbol{\nabla} \rho_i / (\mu_i \rho_{i,un} \rho_i)$. Equivalently to the incompressible case in the main text, we impose continuity of pressure and

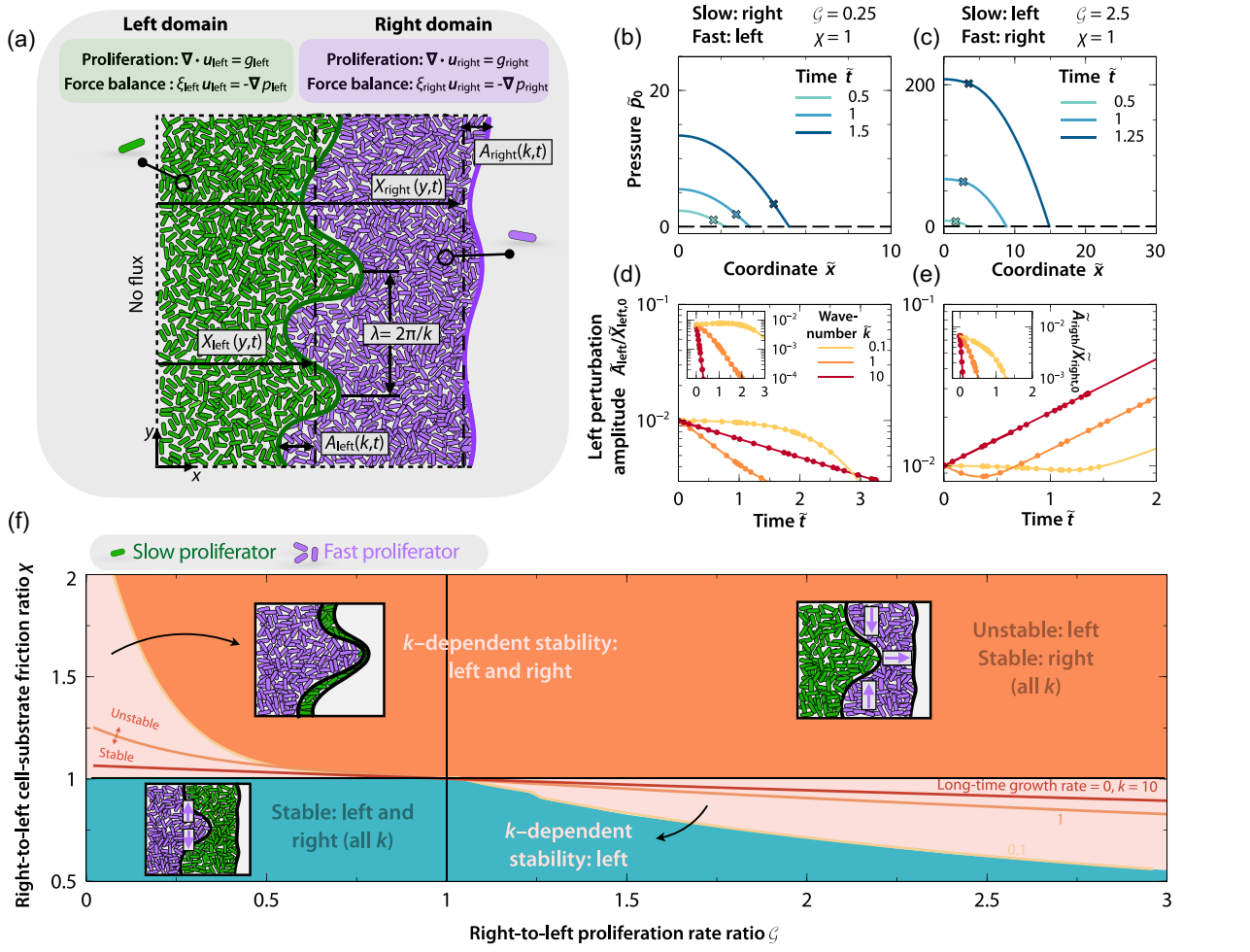


FIG. 8. Model predictions for a community with $\mathcal{R} = 1.5$ show qualitatively similar results to those for the community with $\mathcal{R} = 1.05$ in Fig. 6. (b)–(e) are identical to (b)–(e) in Fig. 6 but for $\mathcal{R} = 1.5$. Similarly, (f) is identical to Fig. 6(f) but for $\mathcal{R} = 1.5$.

velocities, and kinematic conditions at both interfaces, and zero pressure at the outermost interface.

To nondimensionalize the new system of equations, we choose the same characteristic scales for the length, velocity, and time. The characteristic pressure scale is modified to $\mu_{\rm in}\rho_{\rm in,un}R^2_{\rm in,init}g_{\rm in}$. Regarding the density scale, we choose $\rho_{\rm i,un}$ for each density field. Using these scales, we obtain the following dimensionless system of equations:

mass conservation :

$$\partial_{\tilde{t}}\tilde{\rho}_{\rm in} = \mathcal{C}\boldsymbol{\nabla}^2\tilde{\rho}_{\rm in} + \tilde{\rho}_{\rm in}, \quad \text{at } 0 \le \tilde{r} \le \tilde{R}_{\rm in}, \tag{C2}$$

$$\partial_{\tilde{t}}\tilde{\rho}_{\rm out} = \frac{\mathcal{C}\mathcal{E}}{\tilde{\chi}}\boldsymbol{\nabla}^2\tilde{\rho}_{\rm out} + \mathcal{G}\tilde{\rho}_{\rm out}, \quad \text{at } \tilde{R}_{\rm in} \le \tilde{r} \le \tilde{R}_{\rm out}; \tag{C3}$$

stress balance:

$$\tilde{\rho}_{\rm in} - 1 = \mathcal{E}(\tilde{\rho}_{\rm out} - 1), \quad \text{at } \tilde{r} = \tilde{R}_{\rm in}, \tag{C4}$$

$$\tilde{\rho}_{\rm out} = 1, \quad \text{at } \tilde{r} = \tilde{R}_{\rm out}; \tag{C5}$$

continuity of velocity:

$$\frac{\boldsymbol{\nabla}\tilde{\rho}_{\rm in}}{\tilde{\rho}_{\rm in}}\cdot\hat{\boldsymbol{n}}_{\rm in} = \frac{\mathcal{E}}{\tilde{\chi}}\frac{\boldsymbol{\nabla}\tilde{\rho}_{\rm out}}{\tilde{\rho}_{\rm out}}\cdot\hat{\boldsymbol{n}}_{\rm in}, \quad \text{at } \tilde{r} = \tilde{R}_{\rm in}; \tag{C6}$$

kinematic condition :

$$\left(\partial_{\tilde{t}}\tilde{\boldsymbol{r}}_{\rm s,in} + \mathcal{C}\frac{\boldsymbol{\nabla}\tilde{\rho}_{\rm in}}{\tilde{\rho}_{\rm in}}\right)\cdot\hat{\boldsymbol{n}}_{\rm in} = 0, \quad \text{at } \tilde{r} = \tilde{R}_{\rm in}, \tag{C7}$$

$$\left(\partial_{\tilde{t}}\tilde{\boldsymbol{r}}_{\rm s,out} + \frac{\mathcal{C}\mathcal{E}}{\tilde{\chi}}\frac{\boldsymbol{\nabla}\tilde{\rho}_{\rm out}}{\tilde{\rho}_{\rm out}}\right)\cdot\hat{\boldsymbol{n}}_{\rm out} = 0, \quad \text{at } \tilde{r} = \tilde{R}_{\rm out}, \tag{C8}$$

where the new key dimensionless parameters are

$$\mathcal{C} \equiv \frac{G_{\rm in}}{\mu_{\rm in}\rho_{\rm in,un}R^2_{\rm in,init}g_{\rm in}} : \frac{\text{inner domain elasticity}}{\text{proliferation pressure}},$$
$$\mathcal{E} \equiv \frac{G_{\rm out}}{G_{\rm in}} : \frac{\text{outer domain elasticity}}{\text{inner domain elasticity}},$$
$$\tilde{\chi} \equiv \frac{\mu_{\rm out}\rho_{\rm out,un}}{\mu_{\rm in}\rho_{\rm in,un}} : \frac{\text{outer domain cell-substrate friction}}{\text{inner domain cell-substrate friction}}. \tag{C9}$$

To test whether a nonuniform cell density affects the interfacial instability, we perform full 2D numerical simulations of Eqs. (C2)–(C8) in the circular geometry, imposing an initially uniform density $\tilde{\rho}_{\rm i} = 1$. For simplicity, we assume that $\tilde{\chi} = 1$ and $\mathcal{E} = 1$, i.e., both domains display the same cell-substrate friction and proliferation pressure-density relation, $\mathcal{C} = 1$, $\mathcal{G} = 2.5$, and $\mathcal{R} = 1.05$ [the same as in Figs. 3(a)–3(c)]. Figure 10 displays snapshots of the cell density field $\tilde{\rho}(\tilde{\boldsymbol{r}}, \tilde{t})$ in both domains at times $\tilde{t} = 0$ (a), $\tilde{t} = 1.4$ (b), and $\tilde{t} = 2.97$ (c). As $\tilde{\rho}$ can vary spatially, the expansion is slower than in the incompressible case. Indeed, while the density increases locally with an exponential form at sufficiently long time, the radii of both domains do not grow exponentially. Moreover, at time $\tilde{t} \gtrsim 1.6$, a high-density ring is created at the contact interface between the two domains (rightmost panels). This high-density region travels outwardly with time, expanding

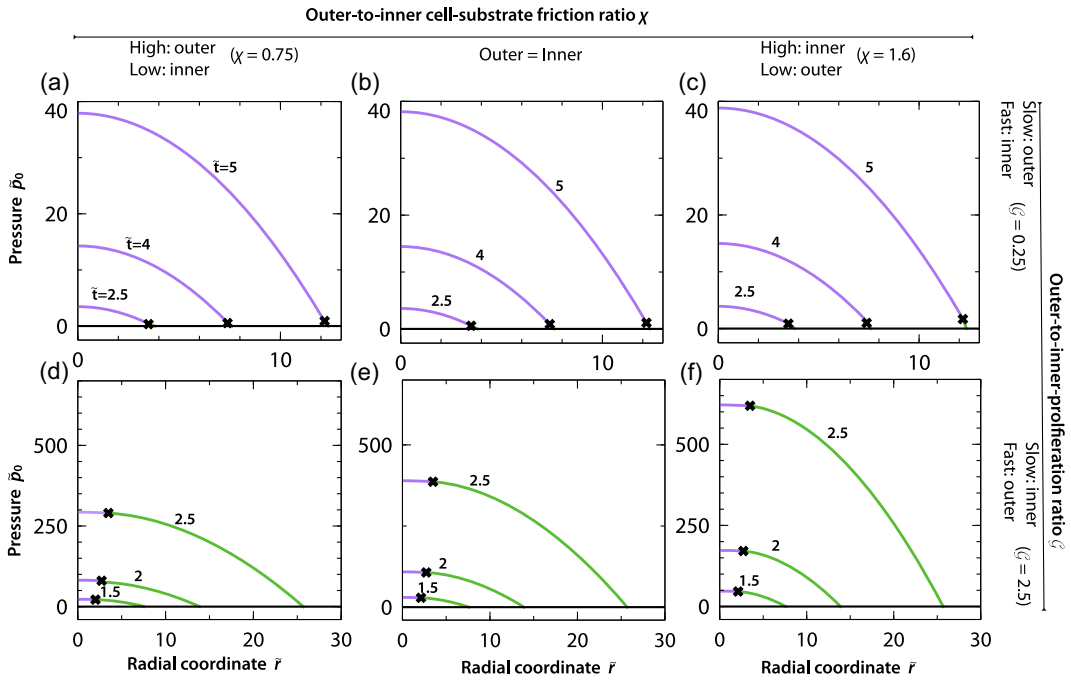


FIG. 9. Base 1D pressure field $\tilde{p}_0$ as a function of the radial coordinate $r$ at different times for $\mathcal{R} = 1.05$ and different values of $\mathcal{G}$ and $\chi$. Crosses indicate the position of the interface between the domains.

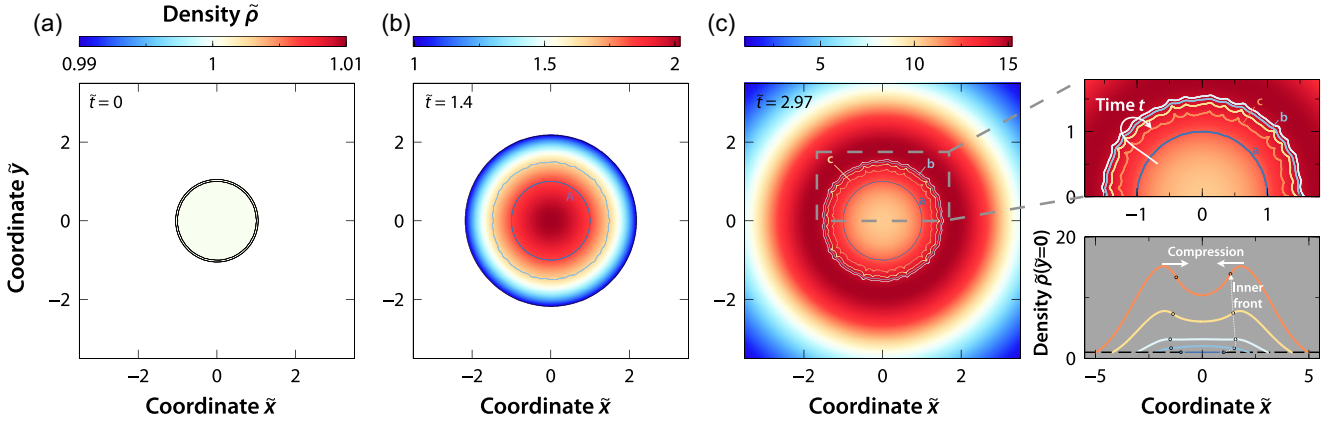


FIG. 10. (a)–(c) Color plots of the density field $\tilde{\rho}(\tilde{\boldsymbol{r}}, \tilde{t})$ for the same values of $\mathcal{G}$ as in Figs. 3(a)–3(c), and $\mathcal{R} = 1.05$, $\mathcal{C} = 1$, $\mathcal{E} = 1$, and $\tilde{\chi} = 1$, at times $\tilde{t} = 0$, 1.4, and 2.97. The rightmost panels show an enlarged view of the density field in (c) (top) and $\tilde{\rho}$ at $\tilde{y} = 0$ as a function of the $\tilde{x}$ coordinate (bottom), also displaying intermediate times.

the outer domain ($\partial_{\tilde{r}}\tilde{\rho} < 0$, $\tilde{\boldsymbol{u}} \cdot \hat{\boldsymbol{e}}_r > 0$) and compressing the inner domain ($\partial_{\tilde{r}}\tilde{\rho} > 0$, $\tilde{\boldsymbol{u}} \cdot \hat{\boldsymbol{e}}_r < 0$). Nonetheless, despite this compression effect whereby the inner interface starts moving inward, the instability remains unaltered as shown in Figs. 10(b) and 10(c), being identical to that of the incompressible case displayed in Figs. 3(a)–3(c). From a biological perspective, the large local increase in cell density shown in Fig. 10 is not realistic. Once the cells are closely packed, the 2D density could not increase as much as we observe in our simulations. Increasing the elastic modulus, considering nutrient-limited growth, and allowing expansion into the third dimension would address this limitation. However, here, we focus on this extreme case to demonstrate that even highly compressible cells would still exhibit the same interface morphodynamics.

## APPENDIX D: NUTRIENT-LIMITED PROLIFERATION DOES NOT PRECLUDE THE MORPHOLOGICAL INSTABILITY

To investigate how nutrient-limited proliferation may influence the interfacial instability, we modify Eqs. (1) and consider a nutrient-dependent proliferation rate given by the Monod equation, i.e., $\boldsymbol{\nabla} \cdot \boldsymbol{u}_i = g_i c_i/(c_{\mathrm{half,i}} + c_i)$, where $c(\boldsymbol{r}, t)$ denotes the local concentration of nutrients at the inner and outer domains. We assume that nutrient dynamics obeys a standard reaction-diffusion equation that incorporates diffusion and uptake in both domains, i.e., $\partial_t c_i = D\boldsymbol{\nabla}^2 c_i - k_i \rho_i c_i/(c_{\mathrm{half,i}} + c_i)$, where $k_i$ is the saturated nutrient uptake rate per cell, $c_{\mathrm{half,i}}$ is the characteristic constant of the Monod equation, and $D$ is the nutrient diffusion coefficient. Moreover, we assume that both cellular proliferation and nutrient uptake obey the same Monod dependence. As for the boundary and initial conditions, we impose a constant concentration of nutrients $c_{\mathrm{out}} = c_0$ at the outer interface $\boldsymbol{r} = \boldsymbol{r}_{\mathrm{s,out}}$, nutrient continuity, i.e., $c_{\mathrm{in}} = c_{\mathrm{out}}$ and $\hat{\boldsymbol{n}}_{\mathrm{in}} \cdot \boldsymbol{\nabla} c_{\mathrm{in}} = \hat{\boldsymbol{n}}_{\mathrm{in}} \cdot \boldsymbol{\nabla} c_{\mathrm{out}}$ at the inner interface $\boldsymbol{r} = \boldsymbol{r}_{\mathrm{s,in}}$, and $c = c_0$ at $t = 0$. We use $c_0$ to nondimensionalize the nutrient concentration, which yields the following dimensionless nutrient equation: $\Gamma \partial_{\tilde{t}} \tilde{c}_i = \boldsymbol{\nabla}^2 \tilde{c}_i - \mathcal{K}_i \tilde{c}_i/(\tilde{c}_{\mathrm{half,i}} + \tilde{c}_i)$, where $\Gamma = R_{\mathrm{in,init}}^2 g_{\mathrm{in}}/D$ compares cellular proliferation and nutrient diffusion timescales, $\mathcal{K}_i = R_{\mathrm{in,init}}^2/\ell_n^2$, compares the initial radius of the inner domain with the nutrient penetration length, $\ell_n = \sqrt{Dc_0/(k_i \rho_i)}$, and $\tilde{c}_{\mathrm{half,i}} = c_{\mathrm{half,i}}/c_0$ compares the half-velocity constant of each domain with the initial nutrient concentration $c_0$.

Figure 11 displays color plots of the local nutrient concentration $\tilde{c}(\tilde{\boldsymbol{r}}, \tilde{t})$ at different times obtained from time-dependent 2D simulations including nutrient diffusion and uptake, using the same values of $\mathcal{G}$, $\chi$, $\mathcal{R}$, $m$, and $\epsilon$ as in Fig. 3. Regarding nutrient-related dimensionless parameters, we consider $\Gamma \ll 1$ and use $\mathcal{K}_{\mathrm{in}} = 0.4$, $\mathcal{K}_{\mathrm{out}} = 1$, and $\tilde{c}_{\mathrm{half,i}} = 1$ for simplicity. As expected, the expansion of both domains slows down as nutrient becomes depleted in their interior, but we find the same type of morphological stability arising at the expanding interface of the inner domain, independent of the values of the dimensionless parameters related to diffusion and uptake. At sufficiently long time, e.g., $\tilde{t} \gtrsim 6$ in Fig. 11, the inner domain stops proliferating as it runs out of nutrients, but the rough interface remains without smoothing out, in agreement with recent experiments [79]. Thus, as expected, nutrient-dependent proliferation modulates only the morphological instability of the inner domain by inhibiting proliferation as nutrient becomes depleted but is not able to stabilize the proliferating interface. Altogether, linear-stability analysis and numerical simulations of our model suggest that such morphological instabilities may be generic, independent of environmental conditions.

Indeed, we take into account the finite amount of nutrients outside the community when performing simulations to recapitulate the expansion dynamics of the multispecies communities shown in Figs. 4(a) and 4(b).

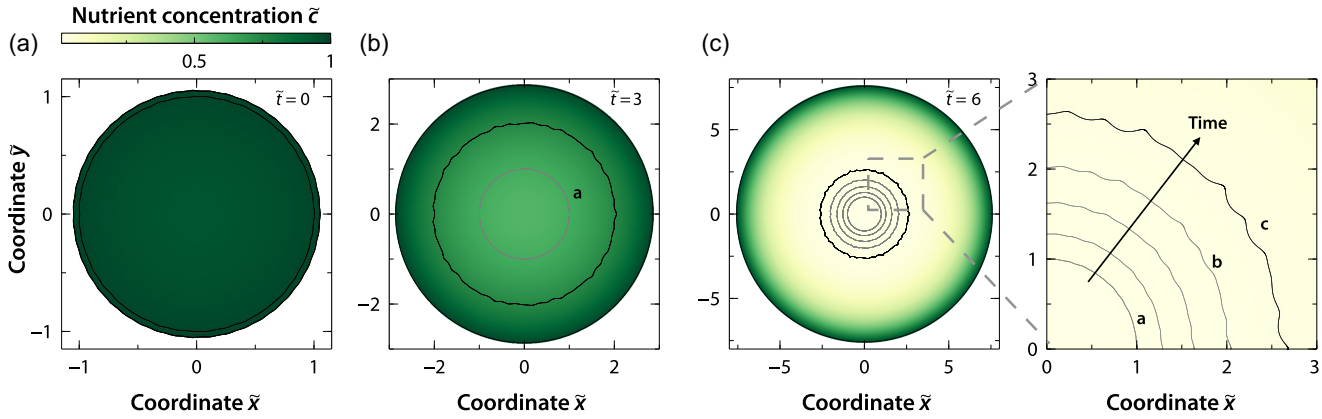


FIG. 11. (a)–(c) Color plots of the 2D nutrient concentration field $\tilde{c}(\tilde{\boldsymbol{r}},\tilde{t})$ for the same values of $\mathcal{G}$ and $\chi$ as in Figs. 3(a)–3(c), $\mathcal{R}=1.05$, $\Gamma \ll 1$, $\mathcal{K}_{\rm in}=0.4$, $\mathcal{K}_{\rm out}=1$, and $\tilde{c}_{\rm half,i}=1$, at times $\tilde{t}=0$, 3, and 6. Grey curves indicate the shape of the inner interface at previous times.

In the experiments, after 30 h, the two species are fully segregated into a core-shell structure and cells become close packed, after which the community begins to expand; we, therefore, consider this time to be the starting time to compare with our model. In the simulations, instead of imposing a fixed nutrient concentration at the outer interface, we also solve the nutrient dynamics outside the community with a no-flux boundary condition at a far-field radius. Hence, $\hat{\boldsymbol{n}}_\infty \cdot \boldsymbol{\nabla}\tilde{c}_{\rm far}=0$ at $\tilde{r}=\tilde{R}_\infty$, where $\tilde{c}_{\rm far}(\boldsymbol{r},t)$ denotes the nutrient concentration field outside the community, which satisfies a conventional 2D diffusion equation without consumption, $\Gamma\partial_{\tilde{t}}\tilde{c}_{\rm far}=\boldsymbol{\nabla}^2\tilde{c}_{\rm far}$. At the outer interface, we also impose nutrient continuity, i.e., $\tilde{c}_{\rm out}=\tilde{c}_{\rm far}$ and $\hat{\boldsymbol{n}}_{\rm out}\cdot\boldsymbol{\nabla}\tilde{c}_{\rm out}=\hat{\boldsymbol{n}}_{\rm out}\cdot\boldsymbol{\nabla}\tilde{c}_{\rm far}$ at $\boldsymbol{r}=\boldsymbol{r}_{\rm s,out}$. In particular, we use the following values of the dimensionless parameters: $\Gamma=0.01$, implying that nutrient diffusion is significantly faster than cellular proliferation, $\mathcal{K}_{\rm i}=0.275$, $\tilde{R}_\infty=15$, and $\tilde{c}_{\rm half,i}=5\times10^{-3}$. The value of $\mathcal{G}$ is 1.6 for the unstable case [Fig. 4(a)] and 0.7 for the stable case [Fig. 4(b)]. Both values are obtained by taking the ratio between the outer and inner proliferation rates, which are extracted from the monoculture expansion dynamics as shown in Fig. 12 (Appendix E).

## APPENDIX E: MEASUREMENTS AND ESTIMATES OF THE DIMENSIONLESS PARAMETERS $\mathcal{G}$ AND $\chi$ FOR PREVIOUSLY PUBLISHED EXPERIMENTS

Here, we detail the reported measurements for $g_{\rm i}$ of the experiments displayed in Fig. 1. These values are used to compute $\mathcal{G}$ and determine the position of each experiment on the state diagram shown in Fig. 5. Regarding values of $\chi$, as detailed in the main text, we consider that $\chi=1$ in all experiments except for Figs. 1(i) and 1(vi). In the experiment shown in Fig. 1(i), the outer domain is a mutant, which exhibits a smaller density of type-IV pili and emerges from the inner domain. As discussed by the authors, the outer domain displays weaker cell-substrate friction, as a consequence of reduced pilus density; thus, we consider $\chi<1$. In the experiment in Fig. 1(vi), the strain in the outer domain is immotile and secretes EPS, while cells in the interior domain are motile and do not secrete EPS; thus, we consider $\chi>1$, as presumably the outer domain exhibits a larger friction with the substrate due to EPS-substrate adhesion. We assume $\chi=1$ for the other experiments in Fig. 1, since the two strains are grown on the same substrate, secrete the same EPS in cases of the biofilm formers, and exhibit the same cell shape.

The experiments displayed in Figs. 1(ii) [79] and 1(iv) [73] are obtained from [73,79]. In these studies the proliferation rates of the two strains are not reported, but we assume that the outer domain outgrows the inner domain as the former keeps proliferating over time, whereas cells of the inner domain stop proliferating or proliferate at a much slower rate, similarly to experiments in Ref. [38]. Experiments displayed by Figs. 1(iii) are from Ref. [83], in which $g_{\rm in}\simeq0.29\ {\rm h}^{-1}$ and $g_{\rm out}\simeq0.58\ {\rm h}^{-1}$; thus, $\mathcal{G}\simeq2$. Regarding the experiment shown in Fig. 1(v) from Ref. [84], $\mathcal{G}\simeq3.5$ obtained from Fig. S2(a) in Ref. [84], and $\chi>1$ since the inner mutant does not secrete EPS, implying a lower substrate friction, while the wild-type strain localized at the outer domain secretes EPS. Another community with the same strains shown in Fig. 2 in Ref. [84], with $\mathcal{G}\simeq6$, also exhibits the same instability. Additionally, Fig. S1 in Ref. [84] also shows a community with $\mathcal{G}\simeq2$ and $\chi>1$ displaying an unstable inner interface. Here, the outer mutant grows faster than the inner mutant and also lacks surfactin secretion, implying a higher friction with the substrate than the inner domain, which in addition lacks EPS secretion. The shapes of these two additional communities are also in agreement with our theory shown in Fig. 5. Finally, $\mathcal{G}\simeq1$ for the experiment shown in Fig. 1(vi) as reported in Ref. [157].

Regarding the experiments from Ref. [59], $g_{\rm in}\simeq0.012\ {\rm h}^{-1}$ and $g_{\rm out}\simeq0.023\ {\rm h}^{-1}$—thus, $\mathcal{G}\simeq1.9$; from Ref. [38],

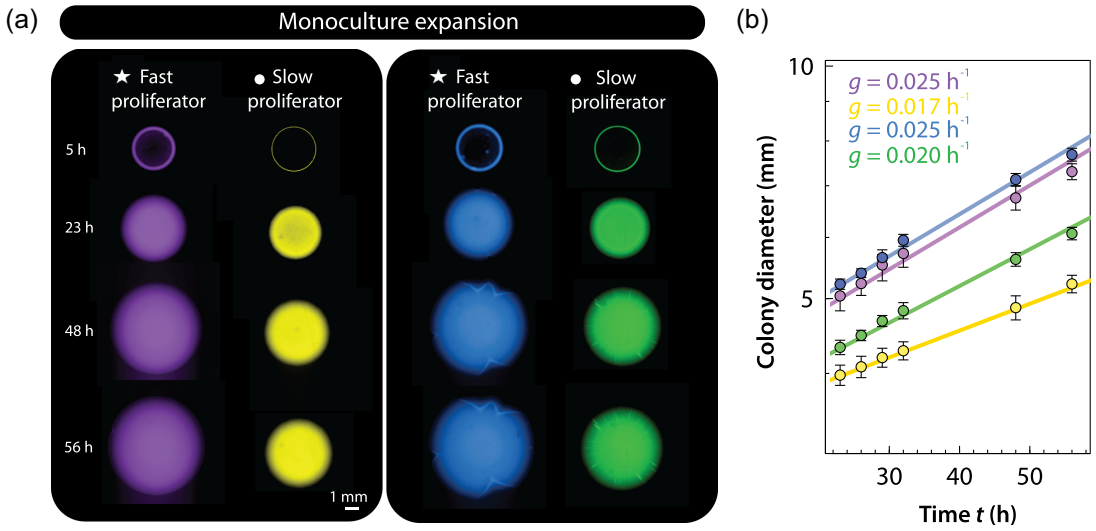


FIG. 12. (a) Monoculture expansions for experiments shown in Fig. 4(a) (left) for *R. planticola* (purple) and *P. rhodesiae* (yellow) and in Fig. 4(b) (right) *R. planticola* (blue) and *P. agglomerans* (green). (b) Single-species colony diameter as a function of time for *R. planticola* (purple), *P. rhodesiae* (yellow), *R. planticola* (blue), and *P. agglomerans* (green). The dots correspond to the experimental measurements, and the solid lines are exponential fits to the experiments, from which the corresponding growth rates $g$ are obtained. The area of each domain is used to determine proliferation rates.

$g_{\rm in} \simeq 0.38\ {\rm h}^{-1}$ and $g_{\rm out} \simeq 0.42\ {\rm h}^{-1}$—thus $\mathcal{G} \simeq 1.11$; from Ref. [39], $\mathcal{G} \simeq 1.1$; and from Ref. [45], $\mathcal{G} \simeq 1.1$–1.2.

To determine the values of $\mathcal{G}$ for the experiments displayed in Fig. 4, we obtain the growth rate of each species from their monoculture expansion, as shown in Fig. 12. We measure the diameter of each single-species colony as a function of time and fit an exponential curve, from which the corresponding growth rate $g$ is obtained. Specifically, we find that $\mathcal{G} \simeq 1.5$–1.6 for the unstable case [Fig. 4(a)] and $\mathcal{G} \simeq 0.8$ for the stable case [Fig. 4(b)]. We consider that all species exhibit the same friction with the substrate, implying $\chi = 1$.

## APPENDIX F: NEW EXPERIMENTS USING BACTERIA ISOLATED FROM SOIL

*R. planticola*, *P. rhodesiae*, and *P. agglomerans* strains were isolated from a soil sample (MIT Killian Court, Cambridge, MA) and were tagged with two different fluorescent proteins mScarlet-I (red) and GFP2 (green) by insertion of plasmids pMRE145 and pMRE132, respectively. For growth substrates, we prepared stiff agar plates with 1X Luria-Bertani media (LB, 2.5% w/v; BD Biosciences-US) and 1.5% w/v of agar (BD Bioscience-US). We also added 1X chloramphenicol (Cm, 15 mg/L, prepared from 1000× solution) for constitutive expression of fluorescence. For each agar plate, 4 mL of media was pipetted into a petri dish (60 × 15 mm, sterile, with vents; Greiner Bio-one) and was cooled overnight (15 h) before inoculation.

At the start of the experiment, for each strain, −80 °C glycerol stock was streaked on a separate plate and proliferated for 2 days. Then, a colony from each strain was picked up and put into a 50 mL Falcon tube filled with 5mL of liquid media (1 × LB and 1× Cm). Bacterial cultures were grown overnight at 30 °C under constant shaking 1350 rpm (on Titramax shakers; Heidolph). We then diluted the cultures to total density of optical density 0.1 ($OD_{600}$) using a Varioskan Flash (Thermo Fisher Scientific) plate reader. The $OD_{600}$-standardized cultures were mixed in 1:1 volume fractions, and we then gently placed a droplet of 1.5 μL inoculant at the center of an agar plate. After inoculation, each community was grown at 30 °C for 120 h. At fixed times after inoculation, each plate was put on a stage of Nikon Eclipse Ti inverted light microscope system. 10× magnification was used for whole-community images. Fluorescent images were taken using Chroma filter sets ET-dsRed (49005) and ET-CFP (49001) and a Pixis 1024 CCD camera.

## APPENDIX G: A CHARACTERISTIC RULE DESCRIBING THE PROGRESSION SPEEDS OF THE DIFFERENT INTERFACES

Our theory enables us to derive a quantitative rule describing the progression speeds of the different interfaces. We derive this rule by comparing the velocities of two circular interfaces:

$$\tilde{u}_{\rm interf,in} = \tilde{\boldsymbol{u}}_{\rm in}(\tilde{r} = \tilde{R}_{\rm in}) \cdot \hat{\boldsymbol{e}}_r = \frac{\tilde{R}_{\rm in}}{2}, \tag{G1a}$$

$$\tilde{u}_{\rm interf,out} = \tilde{\boldsymbol{u}}_{\rm out}(\tilde{r} = \tilde{R}_{\rm out}) \cdot \hat{\boldsymbol{e}}_r = \mathcal{G}\frac{\tilde{R}_{\rm out}}{2} + (1-\mathcal{G})\frac{\tilde{R}_{\rm in}}{\tilde{R}_{\rm out}}. \tag{G1b}$$

The ratio between the two velocities is then given by a simple relation:

$$\frac{\tilde{u}_{\mathrm{interf,out}}}{\tilde{u}_{\mathrm{interf,in}}} = \mathcal{G}\frac{\tilde{R}_{\mathrm{out}}}{\tilde{R}_{\mathrm{in}}} + (1-\mathcal{G})\frac{\tilde{R}_{\mathrm{in}}}{\tilde{R}_{\mathrm{out}}}. \tag{G2}$$

Thus, when $\mathcal{G} < 1$ as in the case in Fig. 2(b), the outer interface moves slower than the inner interface ($\tilde{u}_{\mathrm{interf,out}}/\tilde{u}_{\mathrm{interf,in}} < 1$), whereas when $\mathcal{G} > 1$ as is the case in Fig. 2(c), the outer interface moves faster than the inner interface ($\tilde{u}_{\mathrm{interf,out}}/\tilde{u}_{\mathrm{interf,in}} > 1$). As a result, the inner interface in Fig. 2(b) ($\mathcal{G} \equiv g_{\mathrm{out}}/g_{\mathrm{in}} = 0.25$) remains close to the outer interface over time, while in Fig. 2(c) ($\mathcal{G} = 2.5$), the outer interface moves faster than the inner.


[1] A. Swidsinski, J. Weber, V. Loening-Baucke, L. P. Hale, and H. Lochs, *Spatial organization and composition of the mucosal flora in patients with inflammatory bowel disease*, Journal of clinical microbiology **43**, 3380 (2005).

[2] J.-M. Monier and S. E. Lindow, *Spatial organization of dual-species bacterial aggregates on leaf surfaces*, Appl. Environ. Microbiol. **71**, 5484 (2005).

[3] S. Mitri, J. B. Xavier, and K. R. Foster, *Social evolution in multispecies biofilms*, Proc. Natl. Acad. Sci. U.S.A. **108**, 10839 (2011).

[4] E. G. Wilbanks, U. Jaekel, V. Salman, P. T. Humphrey, J. A. Eisen, M. T. Facciotti, D. H. Buckley, S. H. Zinder, G. K. Druschel, D. A. Fike *et al.*, *Microscale sulfur cycling in the phototrophic pink berry consortia of the sippewissett salt marsh*, Environ. Microbiol. **16**, 3398 (2014).

[5] C. D. Nadell, K. Drescher, and K. R. Foster, *Spatial structure, cooperation and competition in biofilms*, Nat. Rev. Microbiol. **14**, 589 (2016).

[6] P. E. Kolenbrander, *Oral microbial communities: Biofilms, interactions, and genetic systems*, Annu. Rev. Microbiol. **54**, 413 (2000).

[7] K. Werdan, S. Dietz, B. Löffler, S. Niemann, H. Bushnaq, R.-E. Silber, G. Peters, and U. Müller-Werdan, *Mechanisms of infective endocarditis: Pathogen-host interaction and risk states*, Nat. Rev. Cardiol. **11**, 35 (2014).

[8] C. M. Dejea, P. Fathi, J. M. Craig, A. Boleij, R. Taddese, A. L. Geis, X. Wu, C. E. D. Shields, E. M. Hechenbleikner, D. L. Huso *et al.*, *Patients with familial adenomatous polyposis harbor colonic biofilms containing tumorigenic bacteria*, Science **359**, 592 (2018).

[9] P. D. Schloss and J. Handelsman, *Toward a census of bacteria in soil*, PLoS Comput. Biol. **2**, e92 (2006).

[10] R. Hayat, S. Ali, U. Amara, R. Khalid, and I. Ahmed, *Soil beneficial bacteria and their role in plant growth promotion: A review*, Ann. Microbiol. **60**, 579 (2010).

[11] K. Drescher, Y. Shen, B. L. Bassler, and H. A. Stone, *Biofilm streamers cause catastrophic disruption of flow with consequences for environmental and medical systems*, Proc. Natl. Acad. Sci. U.S.A. **110**, 4345 (2013).

[12] R. Rusconi, M. Garren, and R. Stocker, *Microfluidics expanding the frontiers of microbial ecology*, Annu. Rev. Biophys. **43**, 65 (2014).

[13] T. Liu, Y. F. Cheng, M. Sharma, and G. Voordouw, *Effect of fluid flow on biofilm formation and microbiologically influenced corrosion of pipelines in oilfield produced water*, J. Pet. Sci. Eng. **156**, 451 (2017).

[14] S. Elias and E. Banin, *Multi-species biofilms: Living with friendly neighbors*, FEMS Microbiol. Rev. **36**, 990 (2012).

[15] O. Rendueles and J.-M. Ghigo, *Multi-species biofilms: How to avoid unfriendly neighbors*, FEMS Microbiol. Rev. **36**, 972 (2012).

[16] G. Gonzalez-Gil and C. Holliger, *Aerobic granules: Microbial landscape and architecture, stages, and practical implications*, Appl. Environ. Microbiol. **80**, 3433 (2014).

[17] O. X. Cordero and M. S. Datta, *Microbial interactions and community assembly at microscales*, Curr. Opin. Microbiol. **31**, 227 (2016).

[18] J. L. Mark Welch, F. E. Dewhirst, and G. G. Borisy, *Biogeography of the oral microbiome: The site-specialist hypothesis*, Annu. Rev. Microbiol. **73**, 335 (2019).

[19] M. J. I. Müller, B. I. Neugeboren, D. R. Nelson, and A. W. Murray, *Genetic drift opposes mutualism during spatial population expansion*, Proc. Natl. Acad. Sci. U.S.A. **111**, 1037 (2014).

[20] W. Liu, T. A. Tokuyasu, X. Fu, and C. Liu, *The spatial organization of microbial communities during range expansion*, Curr. Opin. Microbiol. **63**, 109 (2021).

[21] A. Prindle, J. Liu, M. Asally, S. Ly, J. Garcia-Ojalvo, and G. M. Süel, *Ion channels enable electrical communication in bacterial communities*, Nature (London) **527**, 59 (2015).

[22] J. Liu, A. Prindle, J. Humphries, M. Gabalda-Sagarra, M. Asally, D.-Y. D. Lee, S. Ly, J. Garcia-Ojalvo, and G. M. Süel, *Metabolic co-dependence gives rise to collective oscillations within biofilms*, Nature (London) **523**, 550 (2015).

[23] J. Humphries, L. Xiong, J. Liu, A. Prindle, F. Yuan, H. A. Arjes, L. Tsimring, and G. M. Süel, *Species-independent attraction to biofilms through electrical signaling*, Cell **168**, 200 (2017).

[24] J. Liu, R. Martinez-Corral, A. Prindle, D.-Y. D. Lee, J. Larkin, M. Gabalda-Sagarra, J. Garcia-Ojalvo, and G. M. Süel, *Coupling between distant biofilms and emergence of nutrient time-sharing*, Science **356**, 638 (2017).

[25] J. W. Larkin, X. Zhai, K. Kikuchi, S. E. Redford, A. Prindle, J. Liu, S. Greenfield, A. M. Walczak, J. Garcia-Ojalvo, A. Mugler *et al.*, *Signal percolation within a bacterial community*, Cell Syst. **7**, 137 (2018).

[26] R. Martinez-Corral, J. Liu, G. M. Süel, and J. Garcia-Ojalvo, *Bistable emergence of oscillations in growing bacillus subtilis biofilms*, Proc. Natl. Acad. Sci. U.S.A. **115**, E8333 (2018).

[27] M. Whiteley, M. G. Bangera, R. E. Bumgarner, M. R. Parsek, G. M. Teitzel, S. Lory, and E. P. Greenberg, *Gene expression in pseudomonas aeruginosa biofilms*, Nature (London) **413**, 860 (2001).

[28] T.-F. Mah, B. Pitts, B. Pellock, G. C. Walker, P. S. Stewart, and G. A. O'Toole, *A genetic basis for pseudomonas aeruginosa biofilm antibiotic resistance*, Nature (London) **426**, 306 (2003).

[29] D. Nguyen, A. Joshi-Datar, F. Lepine, E. Bauerle, O. Olakanmi, K. Beer, G. McKay, R. Siehnel, J. Schafhauser,

Y. Wang *et al.*, *Active starvation responses mediate antibiotic tolerance in biofilms and nutrient-limited bacteria*, Science **334**, 982 (2011).
[30] W. O. H. Hughes and J. J. Boomsma, *Genetic diversity and disease resistance in leaf-cutting ant societies*, Evolution **58**, 1251 (2004).
[31] A. R. Hughes, B. D. Inouye, M. T. J. Johnson, N. Underwood, and M. Vellend, *Ecological consequences of genetic diversity*, Ecol. Lett. **11**, 609 (2008).
[32] T. B. H. Reusch, A. Ehlers, A. Hämmerli, and B. Worm, *Ecosystem recovery after climatic extremes enhanced by genotypic diversity*, Proc. Natl. Acad. Sci. U.S.A. **102**, 2826 (2005).
[33] O. Hallatschek, P. Hersen, S. Ramanathan, and D. R. Nelson, *Genetic drift at expanding frontiers promotes gene segregation*, Proc. Natl. Acad. Sci. U.S.A. **104**, 19926 (2007).
[34] O. Hallatschek and D. R. Nelson, *Gene surfing in expanding populations*, Theor. Popul. Biol. **73**, 158 (2008).
[35] O. Hallatschek and D. R. Nelson, *Life at the front of an expanding population*, Evolution **64**, 193 (2010).
[36] K. S. Korolev, M. Avlund, O. Hallatschek, and D. R. Nelson, *Genetic demixing and evolution in linear stepping stone models*, Rev. Mod. Phys. **82**, 1691 (2010).
[37] F. D. Farrell, M. Gralka, O. Hallatschek, and B. Waclaw, *Mechanical interactions in bacterial colonies and the surfing probability of beneficial mutations*, J. R. Soc. Interface **14**, 20170073 (2017).
[38] A. Giometto, D. R. Nelson, and A. W. Murray, *Physical interactions reduce the power of natural selection in growing yeast colonies*, Proc. Natl. Acad. Sci. U.S.A. **115**, 11448 (2018).
[39] J. Kayser, C. F. Schreck, M. Gralka, D. Fusco, and O. Hallatschek, *Collective motion conceals fitness differences in crowded cellular populations*, Nat. Ecol. Evol. **3**, 125 (2019).
[40] C. Gopalakrishnappa, K. Gowda, K. H. Prabhakara, and S. Kuehn, *An ensemble approach to the structure-function problem in microbial communities*, iScience **25**, 103761 (2022).
[41] K. Gowda, D. Ping, M. Mani, and S. Kuehn, *Genomic structure predicts metabolite dynamics in microbial communities*, Cell **185**, 530 (2022).
[42] S. A. Wilbert and D. K. Newman, *The contrasting roles of nitric oxide drive microbial community organization as a function of oxygen presence*, Curr. Biol. **32**, 5221 (2022).
[43] J. B. Winans, B. R. Wucher, and C. D. Nadell, *Multispecies biofilm architecture determines bacterial exposure to phages*, PLoS Biol. **20**, e3001913 (2022).
[44] B. R. Wucher, J. B. Winans, M. Elsayed, D. E. Kadouri, and C. D. Nadell, *Breakdown of clonal cooperative architecture in multispecies biofilms and the spatial ecology of predation*, Proc. Natl. Acad. Sci. U.S.A. **120**, e2212650120 (2023).
[45] M. Gralka, F. Stiewe, F. Farrell, W. Möbius, B. Waclaw, and O. Hallatschek, *Allele surfing promotes microbial adaptation from standing variation*, Ecol. Lett. **19**, 889 (2016).
[46] Hiroshi Fujikawa and Mitsugu Matsushita, *Fractal growth of bacillus subtilis on agar plates*, J. Phys. Soc. Jpn. **58**, 3875 (1989).
[47] E. Ben-Jacob, H. Shmueli, O. Shochet, and A. Tenenbaum, *Adaptive self-organization during growth of bacterial colonies*, Physica (Amsterdam) **187A**, 378 (1992).
[48] E. Ben-Jacob, O. Schochet, A. Tenenbaum, I. Cohen, A. Czirok, and T. Vicsek, *Generic modelling of cooperative growth patterns in bacterial colonies*, Nature (London) **368**, 46 (1994).
[49] J. A. Shapiro, *The significances of bacterial colony patterns*, BioEssays **17**, 597 (1995).
[50] D. A. Kessler and H. Levine, *Fluctuation-induced diffusive instabilities*, Nature (London) **394**, 556 (1998).
[51] M. Matsushita, J. Wakita, H. Itoh, I. Rafols, T. Matsuyama, H. Sakaguchi, and M. Mimura, *Interface growth and pattern formation in bacterial colonies*, Physica (Amsterdam) **249A**, 517 (1998).
[52] E. Ben-Jacob, I. Cohen, and H. Levine, *Cooperative self-organization of microorganisms*, Adv. Phys. **49**, 395 (2000).
[53] A. Seminara, T. E. Angelini, J. N. Wilking, H. Vlamakis, S. Ebrahim, R. Kolter, D. A. Weitz, and M. P. Brenner, *Osmotic spreading of bacillus subtilis biofilms driven by an extracellular matrix*, Proc. Natl. Acad. Sci. U.S.A. **109**, 1116 (2012).
[54] C. Fei, S. Mao, J. Yan, R. Alert, H. A. Stone, B. L. Bassler, N. S. Wingreen, and A. Košmrlj, *Nonuniform growth and surface friction determine bacterial biofilm morphology on soft substrates*, Proc. Natl. Acad. Sci. U.S.A. **117**, 7622 (2020).
[55] L. Xiong, Y. Cao, R. Cooper, W.-J. Rappel, J. Hasty, and L. Tsimring, *Flower-like patterns in multi-species bacterial colonies*, eLife **9**, e48885 (2020).
[56] J. B. Xavier and K. R. Foster, *Cooperation and conflict in microbial biofilms*, Proc. Natl. Acad. Sci. U.S.A. **104**, 876 (2007).
[57] H. Koo, J. Xiao, M. I. Klein, and J. G. Jeon, *Exopolysaccharides produced by streptococcus mutans glucosyltransferases modulate the establishment of microcolonies within multispecies biofilms*, J. Bacteriol. **192**, 3024 (2010).
[58] Neil J. Buttery, Chandra N. Jack, Boahemaa Adu-Oppong, Kate T. Snyder, Christopher R. L. Thompson, David C. Queller, and Joan E. Strassmann, *Structured growth and genetic drift raise relatedness in the social amoeba dictyostelium discoideum*, Biol. Lett **8**, 794 (2012).
[59] J. David Van Dyken, Melanie J. I. Müller, Keenan M. L. Mack, and Michael M. Desai, *Spatial population expansion promotes the evolution of cooperation in an experimental prisoner's dilemma*, Curr. Biol. **23**, 919 (2013).
[60] W. Kim, F. Racimo, J. Schluter, S. B. Levy, and K. R. Foster, *Importance of positioning for microbial evolution*, Proc. Natl. Acad. Sci. U.S.A. **111**, E1639 (2014).
[61] E. R. Oldewurtel, N. Kouzel, L. Dewenter, K. Henseler, and B. Maier, *Differential interaction forces govern bacterial sorting in early biofilms*, eLife **4**, e10811 (2015).
[62] W. Pönisch, C. A. Weber, G. Juckeland, N. Biais, and V. Zaburdaev, *Multiscale modeling of bacterial colonies: How pili mediate the dynamics of single cells and cellular aggregates*, New J. Phys. **19**, 015003 (2017).
[63] Thibault Stalder and Eva Top, *Plasmid transfer in biofilms: A perspective on limitations and opportunities*, npj Biofilms Microbiomes **2**, 1 (2016).

[64] J. L. Mark Welch, B. J. Rossetti, C. W. Rieken, F. E. Dewhirst, and G. G. Borisy, *Biogeography of a human oral microbiome at the micron scale*, Proc. Natl. Acad. Sci. U.S.A. **113**, E791 (2016).

[65] F. Goldschmidt, R. R. Regoes, and D. R. Johnson, *Successive range expansion promotes diversity and accelerates evolution in spatially structured microbial populations*, ISME J. **11**, 2112 (2017).

[66] J. Yan, C. D. Nadell, H. A. Stone, N. S. Wingreen, and B. L. Bassler, *Extracellular-matrix-mediated osmotic pressure drives vibrio cholerae biofilm expansion and cheater exclusion*, Nat. Commun. **8**, 1 (2017).

[67] W. P. J. Smith, Y. Davit, J. M. Osborne, W. Kim, K. R. Foster, and J. M. Pitt-Francis, *Cell morphology drives spatial patterning in microbial communities*, Proc. Natl. Acad. Sci. U.S.A. **114**, 280 (2017).

[68] W. Pönisch, K. B. Eckenrode, K. Alzurqa, H. Nasrollahi, C. Weber, V. Zaburdaev, and N. Biais, *Pili mediated intercellular forces shape heterogeneous bacterial microcolonies prior to multicellular differentiation*, Sci. Rep. **8**, 1 (2018).

[69] D. S. Glass and I. H. Riedel-Kruse, *A synthetic bacterial cell-cell adhesion toolbox for programming multicellular morphologies and patterns*, Cell **174**, 649 (2018).

[70] J. J. Dong and S. Klumpp, *Simulation of colony pattern formation under differential adhesion and cell proliferation*, Soft Matter **14**, 1908 (2018).

[71] W. Liu, S. Jacquiod, A. Brejnrod, J. Russel, M. Burmølle, and S. J. Sørensen, *Deciphering links between bacterial interactions and spatial organization in multispecies biofilms*, ISME J. **13**, 3054 (2019).

[72] W. Liu, J. Cremer, D. Li, T. Hwa, and C. Liu, *An evolutionarily stable strategy to colonize spatially extended habitats*, Nature (London) **575**, 664 (2019).

[73] S. C. Booth and S. A. Rice, *Influence of interspecies interactions on the spatial organization of dual species bacterial communities*, Biofilm **2**, 100035 (2020).

[74] Sebastian Gude, Erçağ Pinçe, Katja M. Taute, Anne-Bart Seinen, Thomas S. Shimizu, and Sander J. Tans, *Bacterial coexistence driven by motility and spatial competition*, Nature (London) **578**, 588 (2020).

[75] B. Maier, *How physical interactions shape bacterial biofilms*, Annu. Rev. Biophys. **50**, 401 (2021).

[76] A. Giometto, D. R. Nelson, and A. W. Murray, *Antagonism between killer yeast strains as an experimental model for biological nucleation dynamics*, eLife **10**, e62932 (2021).

[77] C. Brooks, M. Yao, J. T. McCool, A. Gillman, G. M. Suel, A. Mugler, and J. W. Larkin, *A computational model of fractal interface formation in bacterial biofilms*, bioRxiv (2024), 10.1101/2022.05.10.491419.

[78] S. Aif, N. Appold, L. Kampman, O. Hallatschek, and J. Kayser, *Evolutionary rescue of resistant mutants is governed by a balance between radial expansion and selection in compact populations*, Nat. Commun. **13**, 1 (2022).

[79] H. Lee, J. Gore, and K. S. Korolev, *Slow expanders invade by forming dented fronts in microbial colonies*, Proc. Natl. Acad. Sci. U.S.A. **119**, e2108653119 (2022).

[80] R. Zöllner, T. Cronenberg, N. Kouzel, A. Welker, M. Koomey, and B. Maier, *Type iv pilin post-translational modifications modulate material properties of bacterial colonies*, Biophys. J. **116**, 938 (2019).

[81] R. Krishna Kumar, T. A. Meiller-Legrand, A. Alcinesio, D. Gonzalez, D. A. I. Mavridou, O. J. Meacock, W. P. J. Smith, L. Zhou, W. Kim, G. S. Pulcu *et al.*, *Droplet printing reveals the importance of micron-scale structure for bacterial ecology*, Nat. Commun. **12**, 1 (2021).

[82] P. R. Secor, L. A. Michaels, D. C. Bublitz, L. K. Jennings, and P. K. Singh, *The depletion mechanism actuates bacterial aggregation by exopolysaccharides and determines species distribution & composition in bacterial aggregates*, Front. Cell. Infect. Microbiol. **12**, 869736 (2022).

[83] R. Tecon and D. Or, *Cooperation in carbon source degradation shapes spatial self-organization of microbial consortia on hydrated surfaces*, Sci. Rep. **7**, 1 (2017).

[84] T. Jautzus, J. van Gestel, and Á. T. Kovács, *Complex extracellular biology drives surface competition during colony expansion in bacillus subtilis*, ISME J. **16**, 2320 (2022).

[85] M. J. Bogdan and T. Savin, *Fingering instabilities in tissue invasion: An active fluid model*, R. Soc. Open Sci. **5**, 181579 (2018).

[86] Y. Guo, M. Nitzan, and M. P. Brenner, *Programming cell growth into different cluster shapes using diffusible signals*, PLoS Comput. Biol. **17**, e1009576 (2021).

[87] M. Martin and T. Risler, *Viscocapillary instability in cellular spheroids*, New J. Phys. **23**, 033032 (2021).

[88] C. A. Safsten, V. Rybalko, and L. Berlyand, *Asymptotic stability of contraction-driven cell motion*, Phys. Rev. E **105**, 024403 (2022).

[89] M. A. Heinrich, R. Alert, A. E. Wolf, A. Košmrlj, and D. J. Cohen, *Self-assembly of tessellated tissue sheets by expansion and collision*, Nat. Commun. **13**, 1 (2022).

[90] D.-Q. Zhang, P.-C. Chen, Z.-Y. Li, R. Zhang, and B. Li, *Topological defect-mediated morphodynamics of active-active interfaces*, Proc. Natl. Acad. Sci. U.S.A. **119**, e2122494119 (2022).

[91] G. A. Stooke-Vaughan and O. Campàs, *Physical control of tissue morphogenesis across scales*, Curr. Opin. Genet. Dev. **51**, 111 (2018).

[92] A. Szabó, E. Theveneau, M. Turan, and R. Mayor, *Neural crest streaming as an emergent property of tissue interactions during morphogenesis*, PLoS Comput. Biol. **15**, e1007002 (2019).

[93] K. Goodwin and C. M. Nelson, *Mechanics of development*, Dev. Cell **56**, 240 (2021).

[94] S. P. Banavar, E. K. Carn, P. Rowghanian, G. Stooke-Vaughan, S. Kim, and O. Campàs, *Mechanical control of tissue shape and morphogenetic flows during vertebrate body axis elongation*, Sci. Rep. **11**, 1 (2021).

[95] R. M. Sutherland, *Cell and environment interactions in tumor microregions: The multicell spheroid model*, Science **240**, 177 (1988).

[96] D. Wirtz, K. Konstantopoulos, and P. C. Searson, *The physics of cancer: The role of physical interactions and mechanical forces in metastasis*, Nat. Rev. Cancer **11**, 512 (2011).

[97] H. Youssefpour, X. Li, A. D. Lander, and J. S. Lowengrub, *Multispecies model of cell lineages and feedback control in solid tumors*, J. Theor. Biol. **304**, 39 (2012).

[98] A. M. Jimenez Valencia, P.-H. Wu, O. N. Yogurtcu, P. Rao, J. DiGiacomo, I. Godet, L. He, M.-H. Lee, D. Gilkes,

S. X. Sun *et al.*, *Collective cancer cell invasion induced by coordinated contractile stresses*, Oncotarget **6**, 43438 (2015).

[99] B. Waclaw, I. Bozic, M. E. Pittman, R. H. Hruban, B. Vogelstein, and M. A. Nowak, *A spatial model predicts that dispersal and cell turnover limit intratumour heterogeneity*, Nature (London) **525**, 261 (2015).

[100] C. D. Paul, W.-C. Hung, D. Wirtz, and K. Konstantopoulos, *Engineered models of confined cell migration*, Annu. Rev. Biomed. Eng. **18**, 159 (2016).

[101] H. Ahmadzadeh, M. R. Webster, R. Behera, A. M. J. Valencia, D. Wirtz, A. T. Weeraratna, and V. B. Shenoy, *Modeling the two-way feedback between contractility and matrix realignment reveals a nonlinear mode of cancer cell invasion*, Proc. Natl. Acad. Sci. U.S.A. **114**, E1617 (2017).

[102] P.-H. Wu, D. M. Gilkes, and D. Wirtz, *The biophysics of 3d cell migration*, Annu. Rev. Biophys. **47**, 549 (2018).

[103] R. Martinez-Garcia, C. E. Tarnita, and J. A. Bonachela, *Spatial patterns in ecological systems: From microbial colonies to landscapes*, Emerg. Top. Life Sci. **6**, 245 (2022).

[104] J. N Wilking, T. E. Angelini, A. Seminara, M. P. Brenner, and D. A. Weitz, *Biofilms as complex fluids*, MRS Bull. **36**, 385 (2011).

[105] M. Schaffner, P. A. Rühs, F. Coulter, S. Kilcher, and A. R. Studart, *3d printing of bacteria into functional complex materials*, Sci. Adv. **3**, eaao6804 (2017).

[106] J. Lu, E. Şimşek, A. Silver, and L. You, *Advances and challenges in programming pattern formation using living cells*, Curr. Opin. Chem. Biol. **68**, 102147 (2022).

[107] H. Kim, D. J. Skinner, D. S. Glass, A. E. Hamby, B. A. R. Stuart, J. Dunkel, and I. H. Riedel-Kruse, *4-bit adhesion logic enables universal multicellular interface patterning*, Nature (London) **608**, 324 (2022).

[108] A. Elosegui-Artola, A. Gupta, A. J. Najibi, B. R. Seo, R. Garry, C. M. Tringides, I. de Lázaro, M. Darnell, W. Gu, Q. Zhou *et al.*, *Matrix viscoelasticity controls spatiotemporal tissue organization*, Nat. Mater. **22**, 117 (2023).

[109] O. Hallatschek, S. S. Datta, K. Drescher, J. Dunkel, J. Elgeti, B. Waclaw, and N. S. Wingreen, *Proliferating active matter*, Nat. Rev. Phys. **5**, 407 (2023).

[110] F. D. C. Farrell, O. Hallatschek, D. Marenduzzo, and B. Waclaw, *Mechanically driven growth of quasi-two-dimensional microbial colonies*, Phys. Rev. Lett. **111**, 168101 (2013).

[111] I. Klapper and J. Dockery, *Finger formation in biofilm layers*, SIAM J. Appl. Math. **62**, 853 (2002).

[112] I. Klapper and J. Dockery, *Mathematical description of microbial biofilms*, SIAM Rev. **52**, 221 (2010).

[113] R. J. Allen and B. Waclaw, *Bacterial growth: A statistical physicist's guide*, Rep. Prog. Phys. **82**, 016601 (2018).

[114] Z. You, D. J. G. Pearce, A. Sengupta, and L. Giomi, *Geometry and mechanics of microdomains in growing bacterial colonies*, Phys. Rev. X **8**, 031065 (2018).

[115] M. R. Mattei, L. Frunzo, B. D'acunto, Y. Pechaud, F. Pirozzi, and G. Esposito, *Continuum and discrete approach in modeling biofilm development and structure: A review*, J. Math. Biol. **76**, 945 (2018).

[116] Y. G. Pollack, P. Bittihn, and R. Golestanian, *A competitive advantage through fast dead matter elimination in confined cellular aggregates*, New J. Phys. **24**, 073003 (2022).

[117] G. T. Fortune, N. M. Oliveira, and R. E. Goldstein, *Biofilm growth under elastic confinement*, Phys. Rev. Lett. **128**, 178102 (2022).

[118] C. Blanch-Mercader and J. Casademunt, *Spontaneous motility of actin lamellar fragments*, Phys. Rev. Lett. **110**, 078102 (2013).

[119] A. Mongera, P. Rowghanian, H. J. Gustafson, E. Shelton, D. A. Kealhofer, E. K. Carn, F. Serwane, A. A. Lucio, J. Giammona, and O. Campàs, *A fluid-to-solid jamming transition underlies vertebrate body axis elongation*, Nature (London) **561**, 401 (2018).

[120] M. R. Warren, H. Sun, Y. Yan, J. Cremer, B. Li, and T. Hwa, *Spatiotemporal establishment of dense bacterial colonies growing on hard agar*, eLife **8**, e41093 (2019).

[121] J. Li, S. K. Schnyder, M. S. Turner, and R. Yamamoto, *Role of the cell cycle in collective cell dynamics*, Phys. Rev. X **11**, 031025 (2021).

[122] Alejandro Martínez-Calvo, Tapomoy Bhattacharjee, R. Kōnane Bay, Hao Nghi Luu, Anna M. Hancock, Ned S. Wingreen, and Sujit S. Datta, *Morphological instability and roughening of growing 3d bacterial colonies*, Proc. Natl. Acad. Sci. U.S.A. **119**, e2208019119 (2022).

[123] H. Darcy, *Les Fontaines Publiques de la Ville de Dijon* (Victor Dalmont, Paris, 1856).

[124] S. Hill, *Channeling in packed columns*, Chem. Eng. Sci. **1**, 247 (1952).

[125] R. L. Chuoke, P. Van Meurs, and C. van der Poel, *The instability of slow, immiscible, viscous liquid-liquid displacements in permeable media*, Trans. Metall. Soc. AIME **216**, 188 (1959).

[126] P. Saffman and G. I. Taylor, *The penetration of a fluid into a porous medium or hele-shaw cell containing a more viscous liquid*, Proc. R. Soc. A **245**, 312 (1958).

[127] D. Bensimon, L. P. Kadanoff, S. Liang, B. I. Shraiman, and C. Tang, *Viscous flows in two dimensions*, Rev. Mod. Phys. **58**, 977 (1986).

[128] G. M. Homsy, *Viscous fingering in porous media*, Annu. Rev. Fluid Mech. **19**, 271 (1987).

[129] M. C. Cross and P. C. Hohenberg, *Pattern formation outside of equilibrium*, Rev. Mod. Phys. **65**, 851 (1993).

[130] D. A. Kessler, J. Koplik, and H. Levine, *Pattern selection in fingered growth phenomena*, Adv. Phys. **37**, 255 (1988).

[131] A. Oron, S. H. Davis, and S. G. Bankoff, *Long-scale evolution of thin liquid films*, Rev. Mod. Phys. **69**, 931 (1997).

[132] The perturbation amplitude of a 2D uniformly proliferating circular domain invading a free space is given by $A = \epsilon \exp[t(1-m)/2]$, where all $m > 1$ modes are stable as $A \to 0$ when $t \gg 1$, and whose 1D radius is $R_0 = \exp(t/2)$, as we showed in previous work [122].

[133] D. Dell'Arciprete, M. L. Blow, A. T. Brown, F. D. C. Farrell, J. S. Lintuvuori, A. F. McVey, D. Marenduzzo, and W. C. K. Poon, *A growing bacterial colony in two dimensions as an active nematic*, Nat. Commun. **9**, 1 (2018).

[134] K. Kawaguchi, R. Kageyama, and M. Sano, *Topological defects control collective dynamics in neural progenitor cell cultures*, Nature (London) **545**, 327 (2017).
[135] A. Doostmohammadi, J. Ignés-Mullol, J. M. Yeomans, and F. Sagués, *Active nematics*, Nat. Commun. **9**, 3246 (2018).
[136] K. Copenhagen, R. Alert, N. S. Wingreen, and Joshua W Shaevitz, *Topological defects promote layer formation in myxococcus xanthus colonies*, Nat. Phys. **17**, 211 (2021).
[137] Eric K Chu, Onur Kilic, Hojung Cho, Alex Groisman, and Andre Levchenko, *Self-induced mechanical stress can trigger biofilm formation in uropathogenic escherichia coli*, Nat. Commun. **9**, 4087 (2018).
[138] Morgan Delarue, Jörn Hartung, Carl Schreck, Pawel Gniewek, Lucy Hu, Stephan Herminghaus, and Oskar Hallatschek, *Self-driven jamming in growing microbial populations*, Nat. Phys. **12**, 762 (2016).
[139] Y. Ye, J. Lin, *Fingering instability accelerates population growth of a proliferating cell collective*, Phys. Rev. Lett. **132**, 018402 (2024).
[140] S. Srinivasan, C. N. Kaplan, and L. Mahadevan, *A multiphase theory for spreading microbial swarms and films*, eLife **8**, e42697 (2019).
[141] Justin Panich, Eric M. Dudebout, Navish Wadhwa, and David F. Blair, *Swashing motility: A novel propulsion-independent mechanism for surface migration in salmonella and e. coli*, bioRxiv, 10.1101/2024.08.21.609010.
[142] F. Beroz, J. Yan, Y. Meir, B. Sabass, H. A. Stone, B. L. Bassler, and N. S. Wingreen, *Verticalization of bacterial biofilms*, Nat. Phys. **14**, 954 (2018).
[143] J. Yan, C. Fei, S. Mao, A. Moreau, N. S. Wingreen, A. Košmrlj, H. A. Stone, and B. L. Bassler, *Mechanical instability and interfacial energy drive biofilm morphogenesis*, eLife **8**, e43920 (2019).
[144] T. Risler, A. Peilloux, and J. Prost, *Homeostatic fluctuations of a tissue surface*, Phys. Rev. Lett. **115**, 258104 (2015).
[145] S. Toda, L. R. Blauch, S. K. Y. Tang, L. Morsut, and W. A. Lim, *Programming self-organizing multicellular structures with synthetic cell-cell signaling*, Science **361**, 156 (2018).
[146] M. Tada, *The morphogenetic changes that lead to cell extrusion in development and cell competition*, Dev. Biol. **477**, 1 (2021).
[147] Stuart A. West, Stephen P. Diggle, Angus Buckling, Andy Gardner, and Ashleigh S. Griffin, *The social lives of microbes*, Annu. Rev. Ecol. Evol. Syst. **38**, 53 (2007).
[148] Ainslie E. F. Little, Courtney J. Robinson, S. Brook Peterson, Kenneth F. Raffa, and Jo Handelsman, *Rules of engagement: Interspecies interactions that regulate microbial communities*, Annu. Rev. Microbiol. **62**, 375 (2008).
[149] Christopher M. Waters and Bonnie L. Bassler, *Quorum sensing: Cell-to-cell communication in bacteria*, Annu. Rev. Cell Dev. Biol. **21**, 319 (2005).
[150] Michael E. Hibbing, Clay Fuqua, Matthew R. Parsek, and S. Brook Peterson, *Bacterial competition: Surviving and thriving in the microbial jungle*, Nat. Rev. Microbiol. **8**, 15 (2010).
[151] Daniel B. Amchin, Jenna A. Ott, Tapomoy Bhattacharjee, and Sujit S. Datta, *Influence of confinement on the spreading of bacterial populations*, PLoS Comput. Biol. **18**, e1010063 (2022).
[152] Robert M. Cooper, Lev Tsimring, and Jeff Hasty, *Interspecies population dynamics enhance microbial horizontal gene transfer and spread of antibiotic resistance*, eLife **6**, e25950 (2017).
[153] K. E. Duncker, Z. A. Holmes, and L. You, *Engineered microbial consortia: Strategies and applications*, Microb. Cell Factories **20**, 1 (2021).
[154] D. Volfson, S. Cookson, J. Hasty, and L. S. Tsimring, *Biomechanical ordering of dense cell populations*, Proc. Natl. Acad. Sci. U.S.A. **105**, 15346 (2008).
[155] P. Recho, J. Ranft, and P. Marcq, *One-dimensional collective migration of a proliferating cell monolayer*, Soft Matter **12**, 2381 (2016).
[156] R. Alert and X. Trepat, *Physical models of collective cell migration*, Annu. Rev. Condens. Matter Phys. **11**, 77 (2020).
[157] C. J. Comerci, A. L. Gillman, L. Galera-Laporta, E. Gutierrez, A. Groisman, J. W. Larkin, J. Garcia-Ojalvo, and G. M. Süel, *Localized electrical stimulation triggers cell-type-specific proliferation in biofilms*, Cell Syst. **13**, 488 (2022).